Ocean Modelling 94 (2015) 46–66

Contents lists available at ScienceDirect

Ocean Modelling

journal homepage: www.elsevier.com/locate/ocemod

Path planning in multi-scale ocean flows: Coordination and dynamic obstacles

T. Lolla*, P.J. Haley Jr., P.F.J. Lermusiaux*

Department of Mechanical Engineering, Massachusetts Institute of Technology, 77 Mass. Ave., Cambridge, MA 02139, United States

ARTICLE INFO

Article history:
Received 10 February 2015
Revised 22 June 2015
Accepted 23 July 2015
Available online 4 August 2015

Keywords:
Ocean forecasting
Coordination
Swarm formation control
Obstacle avoidance
Level-set
Time optimal path planning
Underwater vehicles
UAV

ABSTRACT

As the concurrent use of multiple autonomous vehicles in ocean missions grows, systematic control for their coordinated operation is becoming a necessity. Many ocean vehicles, especially those used in longer-range missions, possess limited operating speeds and are thus sensitive to ocean currents. Yet, the effect of currents on their trajectories is ignored by many coordination techniques. To address this issue, we first derive a rigorous level-set methodology for distance-based coordination of vehicles operating in minimum time within strong and dynamic ocean currents. The new methodology integrates ocean modeling, time-optimal level-sets and optimization schemes to predict the ocean currents, the short-term reachability sets, and the optimal headings for the desired coordination. Schemes are developed for dynamic formation control, where multiple vehicles achieve and maintain a given geometric pattern as they carry out their missions. To do so, a new score function that is suitable for regular polygon formations is obtained. Secondly, we obtain an efficient, non-intrusive technique for level-set-based time-optimal path planning in the presence of moving obstacles. The results are time-optimal path forecasts that rigorously avoid moving obstacles and sustain the desired coordination. They are exemplified and investigated for a variety of simulated ocean flows. A wind-driven double-gyre flow is used to study time-optimal dynamic formation control. Currents exiting an idealized strait or estuary are employed to explore dynamic obstacle avoidance. Finally, results are analyzed for the complex geometry and multi-scale ocean flows of the Philippine Archipelago.

© 2015 Elsevier Ltd. All rights reserved.

1. Introduction and motivation

The simultaneous use of multiple agents enables complex tasks to be completed in a coordinated and robust manner. In nature, coordination is commonly exhibited by bees, birds, ants, and other animals when they perform activities such as foraging, navigation and hunting. Coordination also improves the overall performance of teams of autonomous robots. Multi-agent systems are then also versatile and effective in completing tasks such as exploring, mapping and monitoring. To execute such tasks, single agent approaches may either be much slower or much more sensitive to disruptions and uncertainties.

Coordination among Autonomous Underwater Vehicles (AUVs) such as gliders and propelled vehicles (including surface crafts such as kayaks) is now feasible in various types of ocean sampling and exploratory missions due to major advances in manufacturing (Yuh, 2000), vehicle reliability (Bahr et al., 2009; Fiorelli et al., 2004), robotics (Bellingham and Rajan, 2007) and autonomy (Curtin and Bellingham, 2009; Curtin et al., 1993; Hagen et al., 2007; Lermusiaux et al., 2015). Equipped with sensors to observe the pertinent ocean features, AUV teams can sample the ocean adaptively (Fiorelli et al., 2004; Leonard et al., 2010; Lermusiaux et al., 2007; Ramp et al., 2009; Smith et al., 2011; Wang et al., 2009), enabling individual units to exploit the information gathered by other group members (Bahr et al., 2009; Paley et al., 2008). To do so, trajectories of underwater vehicles need to be planned, which is challenging. As AUVs are susceptible to ocean currents, their trajectories can be greatly influenced by the flows they encounter (Lolla et al., 2014a; 2014b). Therefore, autonomous planning should account for predicted currents, especially when they are strong and dynamic. Additionally, AUVs often operate in sea environments with physical obstacles or with 'forbidden' regions, either of which can be dynamic. As a result, ideal autonomous coordination should integrate ocean modeling with sensing, planning, control, estimation and optimization.

As ocean flows are characterized by numerous spatial and temporal scales, multi-vehicle tasks also encompass a wide range of scales. In our applications, vehicles scales (meter and second) are assumed shorter and faster than the flow scales of interest. Nonetheless, for smaller-scale ocean missions, specific vehicle speeds and pattern formations can be critical. When a group must function as a

* Corresponding authors. Tel.: +1 617 324 5172; fax: +1 617 324 3541.
E-mail addresses: ltapovan@mit.edu (T. Lolla), phaley@mit.edu (P.J. Haley Jr.), pierrel@mit.edu (P.F.J. Lermusiaux).

http://dx.doi.org/10.1016/j.ocemod.2015.07.013
1463-5003/© 2015 Elsevier Ltd. All rights reserved.

communication network, spatial scales are limited by transmission losses that increase with range. Small sampling scales are also needed to characterize sub-mesoscale or turbulent features such as microstructures, eddies and algae patches. In larger-scale missions, underwater vehicle-to-vehicle communication may be impractical. One may then be interested in optimizing the endurance of the swarm (Subramani et al., 2015) or in observing ocean processes such as mesoscale fronts, coastal upwelling and relaxation events, basin-scale current systems or coherent structures (Haley et al., 2009; Michini et al., 2014; Reed and Hover, 2014; 2013; Rudnick et al., 2004; Schmidt et al., 1996; Schofield et al., 2010). Similarly, for other sampling applications, either slow or fast temporal scales may drive the mission (Fiorelli et al., 2004; Leonard et al., 2007).

This paper presents a methodology for distance-based coordination of underwater vehicles operating in minimum-time within multi-scale ocean flows, combining ocean modeling with a level-set approach and optimization for coordinated motions. A critical question is: can a group of AUVs be controlled to form and maintain prescribed shapes or patterns while carrying out a mission, regardless of the ocean currents?; and if so, how? The goal of formation control, a specific type of distance-based coordination, is to have a group of vehicles organize into stable patterns, including geometrical shapes such as triangles, squares, or lines. Presently, we combine such coordination with time-optimal path planning. Applications include transportation, surveillance, exploration, inspection and distributed sensing (Jouvencel et al., 2010; Lolla, 2012; Mallory et al., 2013). While single-vehicle missions provide local data on currents, temperature and salinity, multi-vehicle missions coordinated through pattern formation enable the direct estimation of gradients and variability, which is fundamental.

A second contribution of this paper is a technique to compute time-optimal trajectories of AUVs operating in the presence of dynamic obstacles and forbidden regions. Obstacles such as islands or ships block the ocean currents as well as the vehicles. However, forbidden regions are open sea regions that the vehicles must avoid. Examples include fishing zones, polluted or dangerous areas, or regions to stay clear of in order to remain undetected. A simple example with stationary forbidden regions was provided in Lolla et al. (2012). Presently, we consider dynamic forbidden regions in realistic settings and develop the solution technique. Such dynamic time-optimal problems amount to a coordination among the AUVs and the variable obstacles.

Pattern formation control (Bendjilali et al., 2009; Swaminathan and Minai, 2005) has algorithms falling broadly into three categories. The first consists of *behavior-based* approaches, in which the desired behaviors (collision avoidance, formation keeping, target seeking etc.) are prescribed to each robot (Arkin and Balch, 1998) and the final robot control is derived by weighing the relative importance of each behavior. This method is flexible and can guide the robots through uncertain environments using only the local sensor information. *Virtual-structure* approaches constitute the second category of formation control algorithms, where the entire group is considered as a virtual rigid structure, so that the whole robotic system is analogous to a physical object (Ren et al., 2003). Trajectories are not assigned to individual robots, but to the entire unit as a whole. In *leader–follower* approaches for formation control, some of the agents are labeled as the *leaders* and their trajectories are precomputed. The remaining vehicles (followers) form and maintain a desired posture around the leaders. Such methods have been widely studied, both for holonomic (Bendjilali et al., 2009; Desai, 2002; Dimarogonas et al., 2009) and non-holonomic (Consolini et al., 2007) robots operating in stationary environments, also considering noisy communications among vehicles (Ren and Sorensen, 2008; Sisto and Gu, 2006). Leader–follower methods are scalable and relatively easy to implement. However, planning follower trajectories that are robust to faults in the leaders' trajectories remains an active challenge. Graph search (Desai, 2002) and potential field methods (Jouvencel et al., 2010) are among the different techniques used to compute the trajectories of the follower vehicles.

Potential field methods for cooperative formation control define artificial force laws between pairs of robots or robot groups in order to attain a prescribed formation (Jouvencel et al., 2010; Reif and Wang, 1999; Yang and Zhang, 2010). Different types of potential-, fluid- and force-fields have been studied (Fierro et al., 2002; Leonard and Fiorelli, 2001; Pimenta et al., 2013; Sabattini et al., 2011; Zhang and Leonard, 2007). Other formation control methods use implicit shape functions (Chaimowicz et al., 2005). In such methods, the desired shape is set as the zero-contour of a suitable function and vehicles are then controlled by a gradient descent technique to achieve the desired shape. The algorithm may be augmented with artificial robot-to-robot repulsion to spread the robots uniformly along the contour. This approach provides flexibility in the formation shape and is suitable for a range of swarm sizes (Esin et al., 2008; Paley et al., 2008; Zhang et al., 2007). Convex optimization techniques for formation control in swarms are discussed in Derenick and Spletzer (2007), and extended to handle dynamic obstacles in Liu et al. (2011). For more reviews on pattern formation control, we refer to Lolla (2012).

In most of the above formation control studies, the kinematics of the vehicles is not affected by the environment. Yet, underwater vehicles have limited operating speeds, and dynamic ocean currents should be accounted for. For time-optimal path planning without coordination, we can utilize recent level-set equations that apply to regular ocean flows (Lolla et al., 2014a; 2014b). However, extending this approach to coordinated path planning is a major challenge. It may require a completely different method or a combination with one of the above-mentioned algorithms. Presently, inspired by fluid and ocean modeling, our aim is to obtain and employ governing principles and equations that lead to coordinated motions under varied flow regimes. A second challenge is how to deal with physical obstacles and dynamic forbidden regions in such coordinated planning, without increasing the computational cost. All of these challenges are addressed next.

In Section 2, we define the notation and briefly review the level-set equations for time-optimal path planning. In Section 3, we show how the approach can be augmented to treat dynamic obstacles and forbidden regions. In Section 4, we extend this approach and obtain a methodology to plan optimal coordinated paths. These results are exemplified using realistic multi-scale ocean flows in Section 5. Conclusions and future work are given in Section 6.

2. Time-optimal path planning using level-set equations

Our results on time-optimal navigation in dynamic ocean flows with moving obstacles and time-optimal coordinated formation control are based on a recent level-set approach (Lolla et al., 2014a; 2014b; 2012). These level-set equations, which can be directly solved for in ocean models, are now outlined. The presentation is limited to two dimensions; the extension to higher dimensions is straightforward.

Let $\Omega \subseteq \mathbb{R}^2$ be an open set. Starting at time $t_s (\geq 0)$, suppose a vehicle (denoted by P) moves in Ω under the influence of a bounded, Lipschitz continuous dynamic flow-field $\mathbf{V}(\mathbf{x}, t) : \Omega \times [0, \infty) \to \mathbb{R}^2$. Let $F > 0$ be the maximum speed of the vehicle relative to the flow. Let the start and end points of the vehicle be denoted by $\mathbf{y}^s$ and $\mathbf{y}^f$ respectively. The trajectory of the vehicle, denoted by $\mathbf{X}_P(t; \mathbf{y}^s, t^s)$ is governed by the kinematic relation

$$\frac{d\mathbf{X}_P}{dt} = F_P(t)\hat{h}(t) + \mathbf{V}(\mathbf{X}_P(t; \mathbf{y}^s, t^s), t), \quad t > t^s, \tag{1}$$

where $F_P(t)$ is the instantaneous relative speed of the vehicle that satisfies $0 \leq F_P(t) \leq F$ and $\hat{h}(t)$ is the unit vector in the steering (heading) direction. Hence, the relative velocity of the vehicle is $F_P(t)\hat{h}(t)$, and

its magnitude is $F_P(t)$. The limiting conditions on $\mathbf{X}_P(t; \mathbf{y}^s, t^s)$ are

$$\mathbf{X}_P(t^s; \mathbf{y}^s, t^s) = \mathbf{y}^s, \quad \mathbf{X}_P(\widetilde{T}(\mathbf{y}^f); \mathbf{y}^s, t^s) = \mathbf{y}^f, \tag{2}$$

where $\widetilde{T}(\mathbf{y}) : \Omega \to \mathbb{R}$ is the first 'arrival time' at point $\mathbf{y}$, i.e., the first time P reaches $\mathbf{y}$. Note that the inertia-free kinematic model (1) for the interaction between the flow and the vehicle is assumed to be adequate as the focus here is on long-duration underwater path planning. The vehicles are treated as point particles as their dimensions are much smaller than the length of their trajectories and the scales of the flows of interest. As in Lolla et al. (2014b), the notation $|\bullet|$ denotes the L^2 norm of $\bullet$.

$F_P(t)$ and $\hat{h}(t)$ together constitute the controls of the vehicle. For any end point $\mathbf{y} \in \Omega$, let $F_P^o(t)$ and $\hat{h}^o(t)$ denote the corresponding optimal controls, i.e., controls that minimize $\widetilde{T}(\mathbf{y})$ subject to (1)–(2). Let this minimum arrival time be denoted by $T^o(\mathbf{y})$, and the resultant optimal trajectory be $\mathbf{X}_P^o(t; \mathbf{y}^s, t^s)$. For the end point $\mathbf{y}^f$, the superscript 'o' on quantities pertaining to the optimal trajectory is replaced by '$\star$'.

2.1. Methodology

The path planning methodology (Lolla et al., 2014b; 2012) relies on the prediction of the time-evolving *forward reachable set* of states, which is the set of all points that can be visited by the vehicle at a given time. Formally, the forward reachable set at time t ($\geq t^s$), denoted by $\mathcal{R}(t; \mathbf{y}^s, t^s)$, is defined as the set of all points $\mathbf{y} \in \Omega$ for which there exist controls $F_P(\tau)$ and $\hat{h}(\tau)$ for $t^s \leq \tau \leq t$ and a resultant trajectory $\widetilde{\mathbf{X}}_P(\tau; \mathbf{y}^s, t^s)$ reaching $\mathbf{y}$, i.e. satisfying (1) with $\widetilde{\mathbf{X}}_P(t; \mathbf{y}^s, t^s) = \mathbf{y}$. The forward reachable set $\mathcal{R}(t; \mathbf{y}^s, t^s)$ includes only those points that can be visited by the vehicle at time t. Its boundary is called the *reachability front*, and is denoted by $\partial\mathcal{R}(t; \mathbf{y}^s, t^s)$. Therefore, for any $\mathbf{y} \in \Omega$, $T^o(\mathbf{y})$ is the first time when $\mathbf{y}$ becomes a member of $\mathcal{R}(t; \mathbf{y}^s, t^s)$, or equivalently, when the reachability front $\partial\mathcal{R}(t; \mathbf{y}^s, t^s)$ first reaches $\mathbf{y}$.

It was shown in Lolla et al. (2014b) that $\mathcal{R}(t; \mathbf{y}^s, t^s)$ is related to the viscosity solution (Crandall and Lions, 1983) of the unsteady Hamilton–Jacobi equation

$$\frac{\partial \phi^o}{\partial t} + F|\nabla \phi^o| + \mathbf{V}(\mathbf{x}, t) \cdot \nabla \phi^o = 0 \text{ in } \Omega \times (t^s, \infty), \tag{3}$$

with initial conditions

$$\phi^o(\mathbf{x}, t^s) = |\mathbf{x} - \mathbf{y}^s|, \quad \mathbf{x} \in \Omega. \tag{4}$$

Specifically, at any time $t \geq t^s$,

$$\mathbf{x} \in \mathcal{R}(t; \mathbf{y}^s, t^s) \iff \phi^o(\mathbf{x}, t) \leq 0, \tag{5}$$

i.e., at every point $\mathbf{x}$ that belongs to the reachable set at time $t \geq t^s$, the function ϕ^o is strictly non-positive. Conversely, any point at which ϕ^o is non-positive also belongs to the reachable set at that time. Eq. (5) also implies that $\phi^o(\mathbf{x}, t) = 0$ for all $\mathbf{x} \in \partial\mathcal{R}(t; \mathbf{y}^s, t^s)$. This close relationship between the reachability front and the zero-level-set of ϕ^o constitutes an implicit representation of $\mathcal{R}(t; \mathbf{y}^s, t^s)$ from the numerical solution of (3)–(4).

In addition to the optimal arrival time $T^o(\mathbf{y})$, ϕ^o yields the optimal controls $F_P^o(t)$, $\hat{h}^o(t)$ and trajectory $\mathbf{X}_P^o(t; \mathbf{y}^s, t^s)$ that lead to $\mathbf{y}$. Indeed, from Lolla et al. (2014b), $\mathbf{X}_P^o(t; \mathbf{y}^s, t^s)$ satisfies the equation $\phi^o(\mathbf{X}_P^o(t; \mathbf{y}^s, t^s), t) = 0$ for all $t^s \leq t \leq T^o(\mathbf{y})$, i.e., vehicles on optimal trajectories always remain on the zero level-set of ϕ^o. The optimal controls are

$$F_P^o(t) = F, \quad \hat{h}^o(t) = \frac{\nabla \phi^o(\mathbf{X}_P^o(t; \mathbf{y}^s, t^s), t)}{|\nabla \phi^o(\mathbf{X}_P^o(t; \mathbf{y}^s, t^s), t)|}, \quad t^s < t < T^o(\mathbf{y}), \tag{6}$$

whenever all the terms are well-defined. Equivalently, if ϕ^o is differentiable at $(\mathbf{X}_P^o(t; \mathbf{y}^s, t^s), t)$ for any $t^s < t < T^o(\mathbf{y})$, then,

$$\frac{\mathrm{d}\mathbf{X}_P^o(t; \mathbf{y}^s, t^s)}{\mathrm{d}t} = F \frac{\nabla \phi^o(\mathbf{X}_P^o(t; \mathbf{y}^s, t^s), t)}{|\nabla \phi^o(\mathbf{X}_P^o(t; \mathbf{y}^s, t^s), t)|} + \mathbf{V}(\mathbf{X}_P^o(t; \mathbf{y}^s, t^s), t), \tag{7}$$

i.e., the optimal steering direction is normal to level-sets of ϕ^o, and the optimal relative speed of the vehicle is the maximum speed F.

2.2. Algorithm

The above equations lead to a natural algorithm for minimum-time path planning, given a problem configuration: ($\mathbf{y}^s$, $\mathbf{y}^f$, F, $\mathbf{V}(\mathbf{x}, t)$, t^s). This predictive algorithm is composed of two steps:

1. **Forward Propagation.** First, the reachability front $\partial\mathcal{R}(t; \mathbf{y}^s, t^s)$ is evolved by solving Eq. (3) forward in time, with initial conditions (4). The front is evolved until it first reaches $\mathbf{y}^f$.
2. **Backward Vehicle Tracking.** At the end of the forward propagation step, the optimal vehicle trajectory $\mathbf{X}_P^\star(t; \mathbf{y}^s, t^s)$ and controls are computed by solving (7) backward in time, starting from $\mathbf{y}^f$ at time $T^\star(\mathbf{y}^f) = T^o(\mathbf{y}^f)$, i.e.,

$$\frac{\mathrm{d}\mathbf{X}_P^\star(t; \mathbf{y}^s, t^s)}{\mathrm{d}t} = -F \frac{\nabla \phi^o(\mathbf{X}_P^\star, t)}{|\nabla \phi^o(\mathbf{X}_P^\star, t)|} - \mathbf{V}(\mathbf{X}_P^\star, t),$$
$$\mathbf{X}_P^\star(T^\star(\mathbf{y}^f); \mathbf{y}^s, t^s) = \mathbf{y}^f. \tag{8}$$

The backward vehicle tracking step is necessary since the initial heading direction, $\hat{h}^o(t^s)$ is not known a priori. In Lolla et al. (2014b); 2012), the level-set method is used to solve (3). As a result, efficient schemes such as the narrow-band method (Adalsteinsson and Sethian, 1995) can be employed in the computations. Moreover, level-set methods are well-known to offer substantial advantages over front tracking or other particle based approaches (Osher and Fedkiw, 2003; Sethian, 1999). The numerical schemes used to solve (3) and (8) are summarized in Appendix A. Finally, we note here that the boundedness assumption for the flow-field $\mathbf{V}(\mathbf{x}, t)$ is only needed for the theoretical guarantees of optimality of the level-set approach outlined above. As such, these bounds are not known a priori, and do not directly influence the algorithms developed in this paper.

3. Time-optimal path planning in the presence of dynamic obstacles

The methodology for time-optimal path planning (Section 2) is now extended to handle moving obstacles and forbidden regions, without any increase in the computational cost. Unlike solid obstacles, forbidden regions (e.g. fishing zones, polluted areas, regulated territories) do not affect the flow-field. It is only the AUVs that cannot operate in such regions. Henceforth, both these types of impediments will usually be simply referred to as obstacles. Our objective then is to rigorously compute the time-optimal trajectories of AUVs, accounting for moving obstacles. As for the ocean flows, we assume here that the dynamics of the obstacles and their variable locations are known prior to the path planning, either exactly or in the form of predictions.

Obstacles can be incorporated in the planning by preventing the reachability front from passing through them. One way to do this is to treat the obstacles as solid boundaries for the level-set evolution (3). When unstructured or body-fitted meshes are available, complex obstacle geometries can be resolved and appropriate boundary conditions can be exactly imposed. However, not only does this limit the usage of structured Cartesian grids, but the process of mesh generation then becomes highly dependent on the variable obstacle geometry. When obstacles are allowed to move, a continuous adaptation of the mesh is needed to conform with the moving domain. Alternately, immersed boundary methods (Mittal and Iaccarino, 2005) can be used. They avoid the complication of adaptive meshing by introducing penalty terms in the governing equations to account for moving obstacles. For further references on handling moving obstacles, we refer to Brown-Dymkoski et al. (2014).

Numerical techniques to handle stationary obstacles in front evolution problems are discussed in Sethian (1999). The underlying idea is to implicitly create a numerical mask by setting the speed of the front to zero inside the obstacles. Extension velocity methods (Adalsteinsson and Sethian, 1999) have also been used to model front

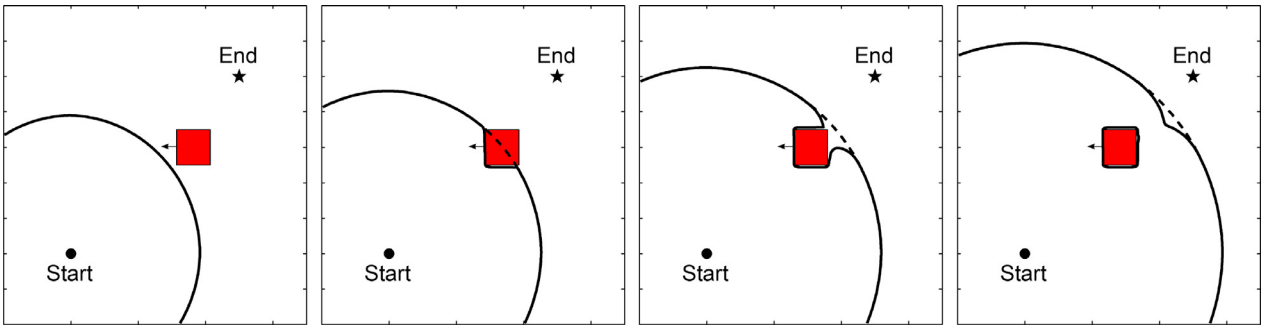

Fig. 1. Time-evolution of the reachability front in the presence of a westward bound square obstacle: The dashed and solid curves depict the reachability fronts obtained by solving Eqs. (3) and (9) respectively. There is no flow in the setup, i.e., $\mathbf{V}(\mathbf{x}, t) = 0$. The original front (dotted) passes through the obstacle whereas the modified one does not. Away from the obstacle, the two fronts coincide.

propagation around obstacles. These methods first generate a discrete approximation of the front and check whether each point on the front is inside or outside the obstacle. Then, the speed function away from the front is appropriately constructed using extension velocities to prevent penetration into the obstacle. In this paper, we extend Sethian's scheme (Sethian, 1999) to address moving obstacles. A first advantage is that no modifications to the numerical grid are required. Secondly, the computational cost remains the same as in the case without obstacles.

Let $\Psi(t)$ and $\mathbf{V}_\Psi(\mathbf{x}, t)$ respectively denote the position and velocity of one obstacle at time t ($\geq t_s$). The reachability front is computed by solving the following modified version of the Hamilton–Jacobi equation (3),

$$\frac{\partial \phi^o}{\partial t} + \widetilde{F}(\mathbf{x}, t)|\nabla \phi^o| + \widetilde{\mathbf{V}}(\mathbf{x}, t) \cdot \nabla \phi^o = 0 \text{ in } \Omega \times (t^s, \infty), \tag{9}$$

where

$$\widetilde{F}(\mathbf{x}, t) = \begin{cases} F, & \text{if } \mathbf{x} \notin \Psi(t), \\ 0, & \text{otherwise}, \end{cases} \tag{10}$$

$$\widetilde{\mathbf{V}}(\mathbf{x}, t) = \begin{cases} \mathbf{V}(\mathbf{x}, t), & \text{if } \mathbf{x} \notin \Psi(t), \\ \mathbf{V}_\Psi(\mathbf{x}, t) & \text{otherwise}. \end{cases} \tag{11}$$

Eq. (9) governs the evolution of the reachability front in the presence of the dynamic obstacle $\Psi(t)$. This equation is obtained by the following modifications inside the obstacle: (i) suppress the normal motion of the front evolution, i.e. $\widetilde{F} = 0$ in (10), and (ii) replace the flow velocity $\mathbf{V}(\mathbf{x}, t)$ with that of the obstacle $\mathbf{V}_\Psi(\mathbf{x}, t)$ in (11). Since these changes are only performed for points inside the obstacle, parts of the reachability front that do not encounter the obstacle remain unaffected. For parts of the front that would otherwise pass through, (10) and (11) reset their velocities to match that of the obstacle. This ensures that no portion of the reachability front penetrates through. For the case of many moving obstacles, one simply uses (9) but modified with a set of Eqs. (10) and (11) for each of the obstacles.

For the numerical implementation, at the beginning of each time-marching step (see Appendix A), grid cells that lie inside the obstacle(s) are identified. The RHS contributions of Eqs. (A.1) and (A.3) are set to zero for such cells. This is equivalent to suppressing the normal motion inside each obstacle ($\widetilde{F} = 0$). Secondly, the flow-field $\mathbf{V}(\mathbf{x}, t)$ in (A.2) at such cells is set to be equal to $\mathbf{V}_\Psi(\mathbf{x}, t)$. The panels of Fig. 1 qualitatively depict the evolution of the reachability front in the presence of a moving obstacle that translates to the left. The reachability front obtained by solving (3) (shown as a dotted line) passes through the obstacle, while that obtained by solving (9) (shown as a solid line) correctly wraps around it. For portions of the front that do not encounter the obstacle, the two reachability fronts coincide. Therefore, the modified evolution Eq. (9) correctly accounts for the obstacle at no additional cost. Other examples using realistic multi-scale ocean flows are provided in Section 5. The next section develops the use of level-set methods for coordination among multiple underwater vehicles.

4. Coordination of underwater vehicles using level-set methods

We now derive a rigorous methodology for distance-based coordination of AUVs operating in minimum-time, within strong and dynamic flows. To do so, we integrate a leader–follower coordination technique with ocean predictions and the above level-set approach (Section 2). The goal is to enable safe, coordinated motion of vehicles in dynamic currents, where the coordination constraints are formulated in the form of relative positions of the vehicles or inter-vehicle spacing during the mission. The critical idea is to utilize and continuously compute the short-time reachability sets of the AUVs in the group. Specifically, the methodology proceeds in two-steps. First, the time-optimal path for the group of vehicles is predicted. Second, as the vehicles progress around this path, their short-time optimal paths are successively computed and optimized as follows: the short-time reachability set for each vehicle in the group is computed. Next, the optimal short-term paths and headings within each of these reachability sets are centrally selected by optimizing the desired coordination function through an exhaustive search. The result is a time-series of short-term paths that most closely sustain the desired coordinated motion throughout the journey. The methodology is general—the governing principles are applicable to swarms of vehicles with varied coordination constraints.

In our presentation next, we focus on formation control for a group of vehicles. The chosen coordination requirement is to achieve and maintain a regular polygon formation (edges of equal length and interior angles of equal measure), where the vehicles occupy the vertices of the polygon. Such regular formations are particularly useful to estimate planar gradients (i.e. equilateral triangle formation), to ensure optimal communication, and for (acoustic) surveillance. It is also applicable to scenarios where the coordinating vehicles must continuously guard a central agent during a mission. Here, we employ a leader–follower description for coordination; nevertheless, this can be easily relaxed to a group-vehicles description.

4.1. Overview

We assume that the group consists of a total of $N_f + 1$ vehicles, for some positive integer N_f. The vehicles are governed by the kinematics (1), and operate in a Lipschitz continuous flow-field $\mathbf{V}(\mathbf{x}, t)$. One of the vehicles in the group is designated to be the *leader* while the remaining N_f vehicles are the *followers*. The start and end points of the leader are denoted as $\mathbf{y}^s$ and $\mathbf{y}^f$ respectively. The followers are numbered 1

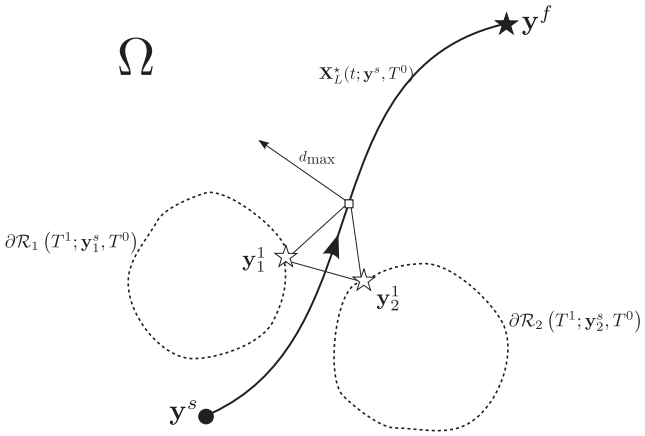

Fig. 2. Schematic of the *pattern optimization* procedure for $N = 2$ and $N_f = 2$: The black curve depicts the time-optimal trajectory of the leader, $\mathbf{X}_L^\star(t;\mathbf{y}^s,T^0)$. Its total travel time is divided into $N = 2$ equal intervals $[T^{i-1},T^i)$, $i = 1, 2$. The intermediate follower reachability fronts, $\partial\mathcal{R}_1(T^1;\mathbf{y}_1^s,T^0)$ and $\partial\mathcal{R}_2(T^1;\mathbf{y}_2^s,T^0)$ are represented by dotted curves. The intermediate follower end points $\mathbf{y}_1^1$ and $\mathbf{y}_2^1$ are determined from the *pattern optimization* (16). The maximum inter-vehicle spacing $d_{\max}$ can be increased to allow for larger-sized patterns (see Remark 6 in Section 4.3).

through N_f and their respective start points are denoted by $\mathbf{y}_k^s$, for $k = 1, 2, \ldots, N_f$. Unlike the leader, the followers are not assigned prespecified end points. As will be shown later, the algorithm optimizes the follower end points, in accord with the coordination constraints, flow-field effects and the leader's trajectory. In what follows, the subscripts L and k are used on quantities pertaining to the leader and the followers respectively.

The minimum travel time $T_L^\star(\mathbf{y}^f)$ and the time-optimal trajectory $\mathbf{X}_L^\star(t;\mathbf{y}^s,0)$ of the leader are first computed by numerically solving (3) and (8). Next, for a chosen positive integer N, the time interval $[0, T_L^\star(\mathbf{y}^f))$ is divided into N disjoint intervals $I^i = [T^{i-1},T^i)$, $i = 1, 2, \ldots, N$ such that $T^0 = 0$, $T^N = T_L^\star(\mathbf{y}^f)$ and $T^i < T^j$ for all $0 \le i < j \le N$. The central idea is to incrementally find intermediate end points for the N_f followers by optimizing a score function that indicates how close the resulting polygon is to being regular (see Fig. 2 for an illustration of this process for $N_f = 2$). These intermediate end points, denoted by $\mathbf{y}_k^i$, $i = 1, 2, \ldots, N$ must be chosen such that the followers can reach them at the times T^i. The duality (5) between reachable sets (fronts) and the viscosity solution to (3) plays an important role in finding the points $\mathbf{y}_k^i$. Once the intermediate end points $\mathbf{y}_k^i$ are known, segments of the follower trajectories spanning time interval I^i are calculated, starting respectively from $\mathbf{y}_k^{i-1}$. By recursion, the complete follower trajectories are determined by the union of their respective segments over all intervals I^i, for $i = 1, 2, \ldots, N$. The equations of this algorithm for formation control are provided next.

4.2. Algorithm

At initial time T^0 (=0), the follower vehicles are respectively located at their start points $\mathbf{y}_k^s$, $k = 1, 2, \ldots, N_f$. We now describe how the follower trajectories over the first time-interval I^1 are computed. To this end, for each k, let ϕ_k^1 be the viscosity solution to the Hamilton–Jacobi Eq. (3) that satisfies the initial condition

$$\phi_k^1(\mathbf{x},0) = |\mathbf{x} - \mathbf{y}_k^s|. \tag{12}$$

The follower reachability fronts at time T^1, denoted by $\partial\mathcal{R}_k(T^1;\mathbf{y}_k^s,T^0)$ are extracted from the fields ϕ_k^1 (each governed by (5)). This can be done using a contour extraction or be part of a narrow band algorithm (Section 4.4). For $k = 1, 2, \ldots, N_f$, the intermediate follower end points $\mathbf{y}_k^1$ are chosen to be points on $\partial\mathcal{R}_k(T^1;\mathbf{y}_k^s,T^0)$ that optimize a coordination function. In our case,

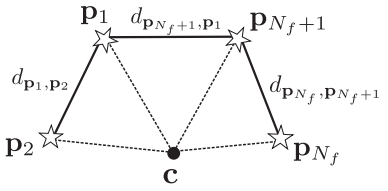

Fig. 3. The polygon $\mathcal{P}$ formed by the vertices $\mathbf{p}_1, \ldots, \mathbf{p}_{N_f+1}$ (star-shaped markers). The geometric centroid is marked as $\mathbf{c}$.

this is a new non-dimensional score function $\gamma : \Omega_{N_f+1} \to [0, 1]$ that we define as follows:

$$\gamma(\mathbf{p}_1,\mathbf{p}_2,\ldots,\mathbf{p}_{N_f+1}) := \max\{\lambda^{\text{side}}\gamma^{\text{side}}(\mathbf{p}_1,\mathbf{p}_2,\ldots,\mathbf{p}_{N_f+1}), \lambda^{\text{angle}}\gamma^{\text{angle}}(\mathbf{p}_1,\mathbf{p}_2,\ldots,\mathbf{p}_{N_f+1})\}, \tag{13}$$

where $\lambda^{\text{side}}, \lambda^{\text{angle}} \in [0, 1]$ are tuning parameters. The functions γ^{side} and γ^{angle} are given by

$$\gamma^{\text{side}}(\mathbf{p}_1,\mathbf{p}_2,\ldots,\mathbf{p}_{N_f+1}) := \frac{\max\{|d_{\mathbf{p}_1,\mathbf{p}_2} - d_{\mathbf{p}_2,\mathbf{p}_3}|, |d_{\mathbf{p}_2,\mathbf{p}_3} - d_{\mathbf{p}_3,\mathbf{p}_4}|, \ldots, |d_{\mathbf{p}_{N_f},\mathbf{p}_{N_f+1}} - d_{\mathbf{p}_{N_f+1},\mathbf{p}_1}|\}}{\max\{d_{\mathbf{p}_1,\mathbf{p}_2}, d_{\mathbf{p}_2,\mathbf{p}_3}, \ldots, d_{\mathbf{p}_{N_f},\mathbf{p}_{N_f+1}}, d_{\mathbf{p}_{N_f+1},\mathbf{p}_1}\}}, \tag{14}$$

$$\gamma^{\text{angle}}(\mathbf{p}_1,\mathbf{p}_2,\ldots,\mathbf{p}_{N_f+1}) := \frac{\max\{|d_{\mathbf{p}_1,\mathbf{c}} - d_{\mathbf{p}_2,\mathbf{c}}|, |d_{\mathbf{p}_2,\mathbf{c}} - d_{\mathbf{p}_3,\mathbf{c}}|, \ldots, |d_{\mathbf{p}_{N_f},\mathbf{c}} - d_{\mathbf{p}_{N_f+1},\mathbf{c}}|\}}{\max\{d_{\mathbf{p}_1,\mathbf{c}}, d_{\mathbf{p}_2,\mathbf{c}}, \ldots, d_{\mathbf{p}_{N_f},\mathbf{c}}, d_{\mathbf{p}_{N_f+1},\mathbf{c}}\}}, \tag{15}$$

where $d_{\mathbf{p},\mathbf{q}} := |\mathbf{p} - \mathbf{q}|$ is the Euclidean distance between $\mathbf{p}$ and $\mathbf{q}$; $\mathbf{c} := \frac{1}{N_f+1}\sum_{\ell=1}^{N_f+1}\mathbf{p}_\ell$ is the geometric centroid of the polygon $\mathcal{P}$ formed by the vertices $\mathbf{p}_1, \mathbf{p}_2, \ldots, \mathbf{p}_{N_f+1}$ arranged in a clockwise or counterclockwise manner (see Fig. 3).

The function γ^{side} represents the maximum normalized difference between adjacent edge lengths of $\mathcal{P}$ and γ^{angle} captures the variation the lengths of the segments connecting the vertices of $\mathcal{P}$ to the centroid $\mathbf{c}$. We note that by construction, for distinct vectors $\mathbf{p}_1, \mathbf{p}_2, \ldots, \mathbf{p}_{N_f+1}$, $0 \le \gamma^{\text{side}}(\mathbf{p}_1,\mathbf{p}_2,\ldots,\mathbf{p}_{N_f+1}) \le 1$. This may be easily verified by observing that each entry in the numerator of (14) is lesser than or equal to the denominator. For instance, $|d_{\mathbf{p}_1,\mathbf{p}_2} - d_{\mathbf{p}_2,\mathbf{p}_3}| \le \max\{d_{\mathbf{p}_1,\mathbf{p}_2}, d_{\mathbf{p}_2,\mathbf{p}_3}\} \le \max\{d_{\mathbf{p}_1,\mathbf{p}_2}, d_{\mathbf{p}_2,\mathbf{p}_3}, \ldots, d_{\mathbf{p}_{N_f},\mathbf{p}_{N_f+1}}, d_{\mathbf{p}_{N_f+1},\mathbf{p}_1}\}$. By a similar argument, it can be shown that $0 \le \gamma^{\text{angle}}(\mathbf{p}_1,\mathbf{p}_2,\ldots,\mathbf{p}_{N_f+1}) \le 1$. For a regular polygon, since all its edges are of equal length and since its vertices are equidistant from the centroid, γ^{side} and γ^{angle} are both zero. γ^{side} tends to 1 when any one side of a regular polygon approaches zero length (i.e., by bringing two adjacent vertices closer to each other). γ^{angle} approaches 1 when a regular polygon is deformed by bringing two opposite vertices close to each other, i.e., by 'squeezing' the polygon. For example, a thin, narrow rhombus has γ^{angle} close to 1. The tuning parameters λ^{side} and λ^{angle} allow us to control the relative importance of γ^{side} and γ^{angle} in the coordination. Since $0 \le \lambda^{\text{side}}, \lambda^{\text{angle}} \le 1$, we deduce using (13), that $0 \le \gamma(\mathbf{p}_1,\mathbf{p}_2,\ldots,\mathbf{p}_{N_f+1}) \le 1$, and that the vertices of a regular polygon minimize γ.

The intermediate follower end points $\mathbf{y}_k^1$, $k = 1, 2, \ldots, N_f$, for I^1 are thus determined from the *pattern optimization*

$$(\mathbf{y}_1^1,\mathbf{y}_2^1,\ldots,\mathbf{y}_{N_f}^1) = \underset{\substack{\mathbf{z}_k\in\partial\mathcal{R}_k(T^1;\mathbf{y}_k^s,T^0),\\ 1\le k\le N_f}}{\arg\min}\ \gamma(\mathbf{X}_L^\star(T^1;\mathbf{y}^s,T^0),\mathbf{z}_1,\mathbf{z}_2,\ldots,\mathbf{z}_{N_f}). \tag{16}$$

The points $\mathbf{y}_k^1$, $k = 1, 2, \ldots, N_f$ are then used to compute $\mathbf{X}_k(t; \mathbf{y}_k^s, T^0)$, the follower trajectory segments over time period I^1 by solving (8), in each case starting at time T^1 and marching backward in time until T^0.

The above steps for I^1 are repeated over each time-period I^i, $i = 1, 2, \ldots, N$, using the intermediate end points $\mathbf{y}_k^i$ as the starting points for the time-period I^{i+1}. Extending (16) to a general $i \geq 1$, we thus obtain

$$(\mathbf{y}_1^{i+1}, \mathbf{y}_2^{i+1}, \ldots, \mathbf{y}_{N_f}^{i+1}) = \underset{\substack{\mathbf{z}_k \in \partial\mathcal{R}_k(T^{i+1}; \mathbf{y}_k^i, T^i), \\ 1 \leq k \leq N_f}}{\arg\min} \gamma(\mathbf{X}_L^\star(T^{i+1}; \mathbf{y}^s, T^0), \mathbf{z}_1, \mathbf{z}_2, \ldots, \mathbf{z}_{N_f}). \tag{17}$$

The follower trajectories over the entire time interval $0 \leq t \leq T_L^\star(\mathbf{y}^f)$ are constructed as the unions of their respective segments over the time-periods I^i. Mathematically, for any t such that $0 \leq t \leq T_L^\star(\mathbf{y}^f)$,

$$\mathbf{X}_k(t; \mathbf{y}_k^s, 0) := \mathbf{X}_k(t; \mathbf{y}_k^i, T^i), \quad k = 1, 2, \ldots, N_f, \tag{18}$$

where $i = \max\{j : T^j \leq t\}$. Therefore, the methodology predicts the trajectories of all the vehicles in the group by solving several smaller path planning problems in succession, optimizing the quality of the formation at the end of each intermediate time interval in an exhaustive fashion. The steps of this formation control scheme are written below in the form of a pseudo-code. Several remarks regarding the algorithm are discussed next.

Algorithm 1 Dynamic formation control using the level-set method.

```
compute T_L^⋆(y^f), X_L^⋆(t; y^s, 0)   ▷ Optimal travel time and path of L
identify T^i, for i = 1, 2, ..., N − 1
set i = 0, y_k^0 = y_k^s, for k = 1, 2, ..., N_f
while i < N, and for each follower k, do   ▷ Follower paths
    solve (3) to compute ∂R_k(T^{i+1}; y_k^i, T^i),
    compute y_k^{i+1} by solving (17) exhaustively
    compute X_k(t; y_k^i, T^i) for t ≤ T^{i+1} by solving (8)
    i ← i + 1
end while
```

4.3. Remarks

(1) *Coordination using the geometric center of mass.* Instead of a leader–follower approach, the algorithm can start by computing the optimal paths for the geometric center of mass of the group (instead of for one of the vehicles). The reachability sets are then computed for all vehicles in the group and the pattern optimization done exhaustively on all vehicles.

(2) *Global optimality and flow variability.* Since our method calculates the short-time (quasi-instantaneous) reachability front for each vehicle, the formation control is *global*, optimizing among all reachable points through an exhaustive search. Hence, it automatically accounts for non-local effects of the variable flow-field and/or any physical obstacles to the vehicle motion. Consequently, no post-processing is needed to account for these effects. This is a key advantage when compared with other coordination schemes that are local and break down if the flow variability is too strong (see the scheme discussed in Appendix B). As a corollary, our short-time reachability sets allow a complete formation control search, regardless of the goal used for the group or leader: for example, if energy minimization is the goal (Subramani et al., 2015), the pattern formation is still optimized within all physically reachable locations at each time.

(3) *Relaxing time-optimality for better formation.* Here, it is assumed that the swarm of vehicles must be navigated in the fastest time, in addition to maintaining a given geometric formation. Time-optimality is guaranteed for the leader, and the follower trajectories are piecewise time-optimal, i.e., each segment of the follower trajectories is time-optimal. When time-optimality is not critical to the mission, the vehicles may be steered at relative speeds lower than F. Their trajectories then, will be governed by suitably modified versions of (3) and (8). This relaxation may facilitate better formation control, at the possible expense of utilizing heuristic schemes for the choice of vehicle speeds. The relative importance of time-optimality and the formation will depend on the requirements of the mission.

(4) *Accuracy of the formation and number N of intermediate times T^is.* The choice of N is dictated by the desired level of accuracy. For small N, few pattern optimizations (17) are performed. The result is still the best possible formation control for that chosen N, but this 'best' could be far from the desired shape for a long time. However, as N is increased, pattern optimizations are performed more frequently, and hence the formation is expected to be more accurately maintained for a longer duration (see Section 5.1 for an illustration). In fact, we show in Section 4.4 that using a large N (time intervals $T^{i+1} - T^i$ of the order of a few CFL time-steps) is numerically cheaper and more accurate.

(5) *Variable resolution with T^i refinements.* There is some flexibility in the choice of the intermediate times T^i. For a given N, one possible choice of T^i is $T^i = \frac{i}{N} \times T_L^\star(\mathbf{y}^f)$, i.e., T^is are equally spaced in the interval $[0, T_L^\star(\mathbf{y}^f)]$. As pattern optimizations are performed at times T^i, T^is may be closely spaced in regions where it is crucial for the formation to be accurately maintained.

(6) *Graph rigidity and the score function γ.* As mentioned earlier, even though the focus here is on the maintenance of any regular polygon formation, this methodology is applicable to other types of formations. For example, specific patterns may be best suited to sense internal waves, fronts or other ocean features. As the dynamic formation control is enforced by optimizing the score function γ, other score functions must be utilized in place of (13) for different coordination criteria. The score function must be designed in such a way that the required pattern is a *unique* minimizer of the function. This issue is closely related to the topic of *graph rigidity* (Olfati-Saber and Murray, 2002; Roth, 1981), where certain score functions may admit multiple optimal configurations. For example, when $N_f = 2$ and $\lambda^{\text{angle}} = 0$ in (13), an equilateral triangle pattern uniquely optimizes (13). However, when $N_f = 3$ and $\lambda^{\text{angle}} = 0$, γ is minimized both by a square pattern and a rhombus pattern. Therefore, if we wish to maintain a regular polygon pattern for $N_f > 2$ it is necessary to set $\lambda^{\text{angle}} > 0$. Hence, care must be taken in designing a score function appropriate for the coordination requirement. Once such a function is found, the methodology presented here can directly be utilized.

(7) *Distance bounds.* The optimization process in (17) may be accelerated by pruning the search space of suitable intermediate end points based on any limits on the separation between the follower vehicles and the leader. In other words, given lower and upper bounds $d_{\min}$, $d_{\max}$ on the permissible distance between the vehicles, points on $\partial\mathcal{R}_k(T^{i+1}; \mathbf{y}_k^s, T^i)$, $k = 1, 2, \ldots, N_f$ that satisfy these constraints may be first identified and the optimization (17) can be then performed over only these points. Furthermore, this technique can be used to detect flow conditions and vehicles for which it is infeasible to maintain formations that satisfy all the distance requirements.

(8) *Deadlock scenarios.* In certain situations, algorithms for formation control may get stuck in a 'deadlock'. Deadlocks often occur when the size of the vehicles is comparable to the

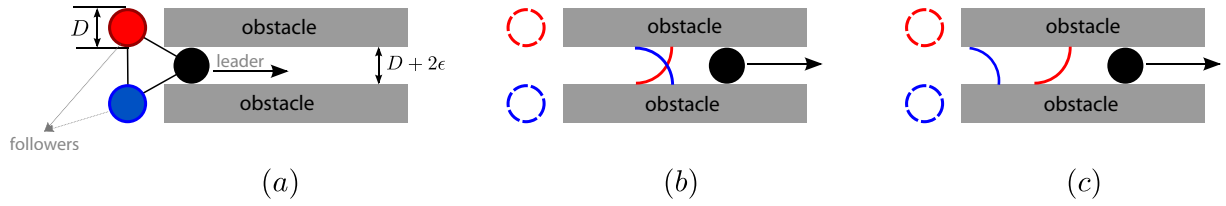

Fig. 4. Example of a deadlock scenario: Three vehicles moving through a narrow passage cannot maintain an equilateral triangle formation as they pass through. The coordination requirement must be relaxed in order for the vehicles to pass.

gaps between obstacles, and the two objectives of maintaining a formation and avoiding obstacles conflict with each other (Shimone et al., 2008; Švestka and Overmars, 1998; Wagner and Choset, 2011). If deadlocks are not resolved, the group may reach an impasse, where vehicles block each other and each vehicle waits for another to make a move. For example, Fig. 4a (Shimone et al., 2008) illustrates a deadlock situation where three vehicles of diameter D, initially in an equilateral triangle formation, must go through a narrow passage. The only way for the vehicles to pass through is to go one after another, temporarily violating the formation requirements. The present work primarily focuses on long-range path planning for underwater vehicles. Here, the vehicles are much smaller in size than the gaps between obstacles (e.g., islands) and hence they are treated as point particles. Our methodology for formation control can be extended to finite-sized vehicles by enforcing minimum separation requirements between pairs of vehicles (see Remark 7, with $d_{\min} \sim D$). Using the example in Fig. 4a, we now briefly explain how our methodology can be used to detect and handle deadlocks. The red and blue curves shown in Fig. 4b represent the segments of the intermediate follower reachability fronts that lie inside the passage. No intermediate end points on both these fronts satisfy all the minimum distance requirements (i.e., stay away from the walls, stay at least distance D away from the leader and from each other). Therefore in this case, the algorithm promptly detects that it is infeasible to maintain the pattern inside the passage. A feasible solution can be obtained by reducing the speed of one of the followers (say, the blue one) and solving suitably modified versions of (3) and (8) for that follower (see Fig. 4c). This allows the red follower to enter the passage behind the leader. Owing to its lower speed, the blue follower is the last to pass through. Once all the vehicles exit the passage, the regular formation control algorithm can be resumed. For other complex formations of finite-sized vehicles in deadlock situations, a systematic procedure of varying the follower vehicle speeds should be employed. However, this is beyond the scope of this paper.

4.3.1. Numerical implementation and complexity

Since the above scheme for formation control involves solving several smaller path planning problems, the overall computational cost is related to that of the level-set method for path planning. A discussion of the asymptotic complexity of the level-set method for path planning is provided in Lolla et al. (2014b). Implementations such as the narrow-band method significantly reduce the asymptotic complexity of the entire algorithm, making it very efficient computationally. Details regarding the numerical solutions of the main governing Eqs. (3) and (8) are provided in Appendix A. We now analyze the asymptotic complexity of our new formation control methodology. This information provides a quantitative basis for selecting a suitable value for N.

4.4. The choice of N based on an asymptotic complexity analysis

In this section, we provide an asymptotic complexity analysis of our dynamic formation control methodology by estimating the number of floating point operations (flops) required by each step of the algorithm. The analysis indicates that when a narrow-band level-set method is used to solve (3), the overall computational cost of the formation control algorithm reduces upon increasing N. We begin by stating the assumptions of this analysis.

4.4.1. Assumptions for flop count estimate

We assume that $\Omega = (0,1)^2$, i.e., the vehicles' motion is restricted to the unit square. The vehicles move in an isotropic manner at a uniform characteristic speed of $\widehat{F}$ (this may correspond to, for example, the sum of F and the average flow speed $|\overline{\mathbf{V}}(\mathbf{x},t)|$). The Hamilton–Jacobi equation governing their reachability front is then

$$\frac{\partial \phi^o}{\partial t} + \widehat{F}|\nabla \phi^o| = 0 \quad \text{in } \Omega \times (0,\infty). \tag{19}$$

The spatial discretization is uniform with n elements in each dimension, corresponding to a grid size of $\Delta x = \Delta y = \frac{1}{n}$. Eq. (19) is solved using a narrow band approach (Adalsteinsson and Sethian, 1995). Reinitialization of the narrow band is also performed, as described in Adalsteinsson and Sethian (1995). The narrow band has a width of d grid elements and is reconstructed when the zero level-set approaches the edge. The time-step is chosen to satisfy CFL stability conditions, i.e., $\Delta t \sim \frac{\Delta x}{\widehat{F}} \sim \frac{1}{n\widehat{F}}$. Assuming the total travel time of the leader is $T_L^\star$, the number of time steps over which (3) is solved for each vehicle is $N_t = \frac{T_L^\star}{\Delta t} = n\widehat{F}T_L^\star$. Finally, we assume that the leader's travel time is divided into N *equal* intervals, each of length $T = \frac{T_L^\star}{N}$.

4.4.2. Complexity analysis for level-set evolution

The numerical computations involved in solving (19) are performed only at grid cells that lie inside the narrow band. We first estimate the number of such grid points at any given time. At any time $t > 0$, the zero level-set of ϕ^o, the viscosity solution to (19) is a circle with radius equal to $\widehat{F}t$. Consequently, the length of the reachability front equals $2\pi\widehat{F}t = \mathcal{O}(\widehat{F}t)$. This implies that the number of grid points inside the narrow band at time t is $\mathcal{O}(\frac{\widehat{F}td}{\Delta x}) = \mathcal{O}(nd\widehat{F}t)$. Hence, the number of flops required to march forward in time from t to $t + \Delta t$ is $\mathcal{O}(nd\widehat{F}t)$. The overall flop count to solve (19) for N_t time steps is:

$$FL_1 = \sum_{i=1}^{N_t} \mathcal{O}(nd\widehat{F}i\Delta t) = \mathcal{O}(nd\widehat{F}N_t^2\Delta t) = \mathcal{O}(n^2\widehat{F}^2T_L^{\star 2}d). \tag{20}$$

4.4.3. Complexity analysis for narrow-band reinitialization

Reinitialization is performed when the front approaches the edge of the narrow band. As the front expands at a characteristic speed of $\widehat{F}$, time interval between successive reinitializations approximately equals $\frac{d\Delta x}{\widehat{F}} = \frac{d}{n\widehat{F}}$. This implies that the narrow band is reinitialized approximately $N_r = \frac{n\widehat{F}T_L^\star}{d}$ times to compute the trajectory of the leader.

The level-set front is first divided several into grid-sized segments. For each such segment, signed distances of all grid points less than d cells away from it are computed. This process is repeated for all segments that constitute the front. For more details, see Adalsteinsson and Sethian (1995). Since the length of the front at time t is $\mathcal{O}(\widehat{F}t)$, the

number of flops needed to reinitialize the narrow band at time t is $\mathcal{O}(d^2 \frac{\widehat{F}t}{\Delta x}) = \mathcal{O}(d^2 \widehat{F} t n)$. The overall reinitialization cost for the leader is obtained by adding the flops required for each reinitialization:

$$FL_2 = \sum_{i=1}^{N_r} \mathcal{O}\left(d^2 \widehat{F} n \left(i \frac{d}{n\widehat{F}} \right) \right) = \mathcal{O}(d^3 N_r^2) = \mathcal{O}(n^2 \widehat{F}^2 T_L^{\star 2} d), \tag{21}$$

which is the same as the cost of level-set evolution (20).

4.4.4. Complexity analysis for pattern optimization

We now estimate the worst case asymptotic complexity of the pattern optimization (17) required to determine the intermediate end points of the follower vehicles. In the absence of a limit on the maximum separation between the vehicles, in the worst case, one needs to search through all points of the intermediate follower reachability fronts to find the optimal intermediate end points. For lengths $l_1, l_2, \ldots, l_{N_f}$ of the intermediate follower reachability fronts, the total worst case complexity of this search is $\mathcal{O}(n^{N_f} \prod_{i=1}^{N_f} l_i)$, assuming the spacing between discrete points of the reachability fronts is comparable to the grid size. The time between successive optimizations is $T = \frac{T_L^\star}{N}$, implying that $l_i = \mathcal{O}(\widehat{F}T)$, which results in $\mathcal{O}(n^{N_f} (\widehat{F}T)^{N_f})$ flops per optimization in the worst case. Hence, the worst case complexity to perform pattern optimizations is

$$FL_3 = \mathcal{O}(n^{N_f} (\widehat{F}T)^{N_f} N).$$

When $d_{\max}$ is the maximum allowable distance between vehicles, segments of the follower reachability fronts that need to be considered for the shape optimization are only $\mathcal{O}(d_{\max})$ in length, as opposed to $\mathcal{O}(\widehat{F}T)$ in the previous paragraph. Utilizing this, the actual worst case complexity for shape optimization is thus:

$$FL_3 = \mathcal{O}(n^{N_f} d_m^{N_f} N), \quad \text{where } d_m = \min(d_{\max}, \widehat{F}T).$$

We note that in the above complexity analysis, we have neglected the computational effort required to identify the parts of the follower reachability fronts that are within a distance $d_{\max}$ away from the leader as this cost varies linearly with the N_f and ceases to be the dominant cost for a larger group of vehicles.

4.4.5. Overall cost and the choice of N

The overall worst case complexity for the pattern formation algorithm is the sum of contributions due to each of the three components discussed above.

$$\begin{aligned} FL &= \underbrace{\mathcal{O}(\widehat{F}^2 n^2 T_L^{\star 2} d)}_{\text{Leader}} + \underbrace{\mathcal{O}(\widehat{F}^2 n^2 T^2 d N N_f) + \mathcal{O}(n^{N_f} d_m^{N_f} N)}_{\text{Followers}} \\ &= \mathcal{O}(\widehat{F}^2 n^2 T_L^{\star 2} d) + \mathcal{O}\left(\widehat{F}^2 n^2 T_L^{\star 2} d \frac{N_f}{N} \right) + \mathcal{O}(n^{N_f} d_m^{N_f} N), \\ d_m &= \min\left(d_{\max}, \frac{\widehat{F} T_L^\star}{N} \right). \end{aligned} \tag{22}$$

As expected, N does not affect the cost incurred to compute the optimal trajectory of the leader. Secondly, it is clear that as N increases, the second term in (22) diminishes. When $\widehat{F}T_L^\star > d_{\max} N$, then $d_m = d_{\max}$, indicating that the pattern optimization cost increases linearly with N. On the other hand when $\widehat{F}T_L^\star < d_{\max} N$, then $d_m = \frac{\widehat{F}T_L^\star}{N}$, from which the overall cost of shape optimization is simplified to $\mathcal{O}\left(\frac{n^{N_f} \widehat{F}^{N_f} T_L^{\star N_f}}{N^{N_f - 1}} \right)$. This cost decreases with increasing N. Hence, the contributions of both the second and third terms of (22) diminish as N increases. This suggests that in order to minimize the overall computational cost, it is better to use a large value for N. We finally note that the above analysis is asymptotic, and that the constant factors in the $\mathcal{O}$ notation become important when the terms in the parentheses are small. Within limits of applicability of such an asymptotic analysis, we conclude that increasing N reduces the computational cost.

A large value of N also forces the pattern optimizations (17) to be performed frequently. As described in Remark 4 of Section 4.3, this also improves the overall coordination and formation control. Therefore, a large N is beneficial both in terms of the quality of the formation and the computational cost. At the limit $N \to \infty$, i.e. continuous optimization in time, the algorithm yields the time-optimal trajectories and the best possible formation control for the desired shape given predicted ocean flows. However, other practical considerations limit how large a value N can take. For example, since the numerical solution of (3) and (8) depends on the resolution (n) and the time step (Δt), N must be small enough so that the successive pattern optimizations are at least a few time steps apart ($T^{i+1} - T^i$ of the order of a few CFL time-steps). This ensures that the intermediate follower reachability fronts are long enough to be resolved by a discrete representation. Furthermore, the choice of N also depends on the curvature of leader's optimal trajectory $\mathbf{X}_L^\star$ and the turning radius of the follower vehicles; N must be small enough such that the follower trajectory segments $\mathbf{X}_k(t; \mathbf{y}_k^i, T^i)$ (see (18)) are at least comparable in length to the vehicles' turning radius. Since the primary focus here is on long-range coordinated path planning, the applications in the following section assume that the turning radius of the vehicles is much smaller than the length of their trajectories.

5. Applications

In what follows, we exemplify our schemes for dynamic formation control and path planning with dynamic obstacles, and analyze their respective results, using several ocean flows. We first consider time-optimal coordinated vehicle motion within an idealized wind-driven double-gyre (Section 5.1). We then demonstrate time-optimal path planning in the presence of moving obstacles within currents exiting an idealized strait or estuary (Section 5.2). Finally, we analyze the results of time-optimal paths with both coordinated motions and dynamic obstacles in a complex realistic ocean region (Section 5.3.3). To do so, we employ data-assimilative two-way nested simulations of multi-scale flows within the Philippine Archipelago.

5.1. Formation control in a wind-driven double-gyre flow

The wind-driven double-gyre simulation is based on the classic idealized model of the ocean circulation engendered by trade winds and mid-latitude easterlies in the northern hemisphere. The wind stresses drive an eastward jet (e.g. the Gulf Stream or Kuroshio), along with a cyclonic gyre and its anti-cyclonic counterpart. The dynamics is governed by a barotropic single-layer model in a square basin of unit size, as described in Dijkstra and Katsman (1997), Simmonet et al. (2009), and Cushman-Roisin and Beckers (2010). The governing non-dimensional Eqs. (23) include the Coriolis force (fu, fv) and idealized wind stress that drive the flow (τ_x, τ_y).

$$\frac{\partial u}{\partial t} = -\frac{\partial p}{\partial x} + \frac{1}{Re}\Delta u - \frac{\partial (u^2)}{\partial x} - \frac{\partial (uv)}{\partial y} + fv + a\tau_x, \tag{23a}$$

$$\frac{\partial v}{\partial t} = -\frac{\partial p}{\partial y} + \frac{1}{Re}\Delta v - \frac{\partial (vu)}{\partial x} - \frac{\partial (v^2)}{\partial y} - fu + a\tau_y, \tag{23b}$$

$$0 = \frac{\partial u}{\partial x} + \frac{\partial v}{\partial y}. \tag{23c}$$

Here, Re is the Reynolds number, $f = \tilde{f} + \beta y$ the non-dimensional Coriolis coefficient, and a is the strength of the wind stress. We use $\tilde{f} = 0$, $\beta = 10^3$, $Re = 150$ and $a = 10^3$, with $\tau_y = 0$ and $\tau_x = -\frac{1}{2\pi}\cos 2\pi y$.

Free-slip boundary conditions are imposed on the north and south walls ($y = 0, 1$) and no-slip boundary conditions on the east and west walls ($x = 0, 1$). A 64×64 grid and a non-dimensional time step of 10^{-4} are used to solve both (23) (generation of flow-field) and (3)

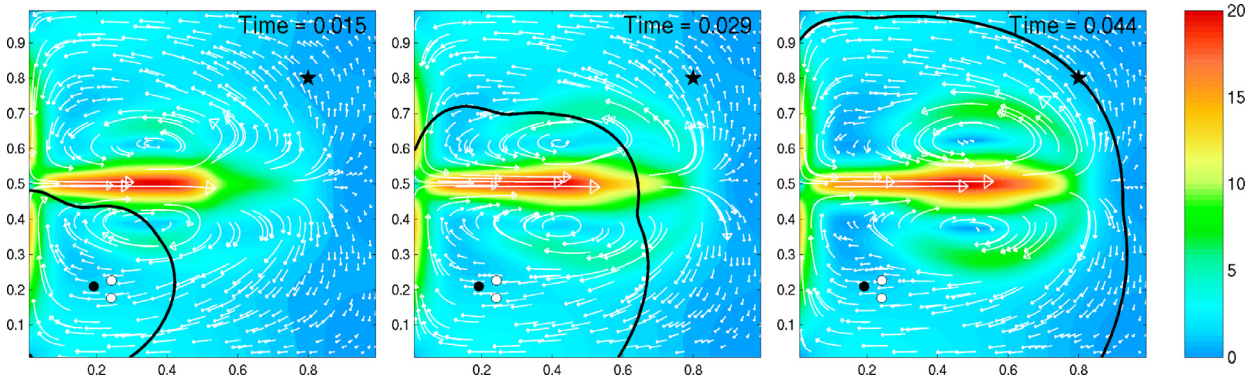

Fig. 5. Evolution of the reachability front (black curve) of the leader vehicle in a double-gyre flow: The start and end points of the leader are represented by shaded round and star markers respectively. The white curved vectors indicate the flow direction/strength and are overlaid on a color plot of the flow magnitude. (For interpretation of the references to color in this figure legend, the reader is referred to the web version of this article.)

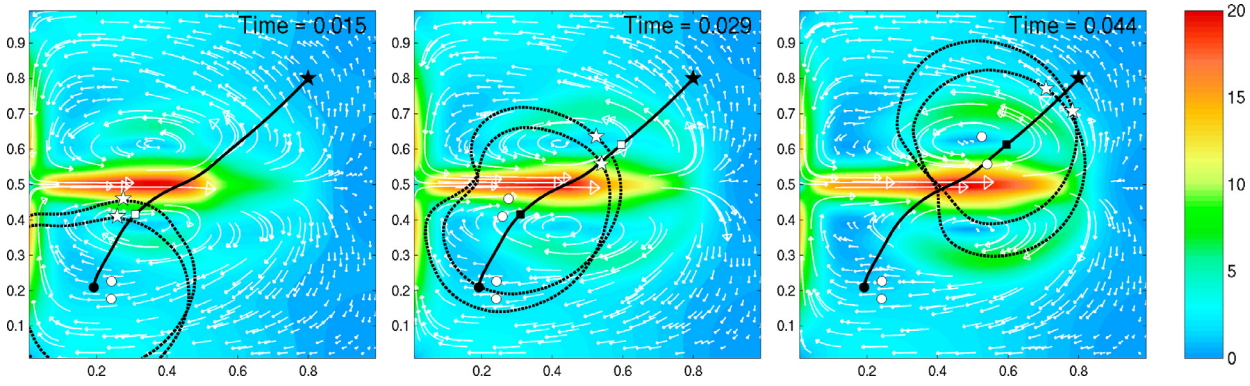

Fig. 6. Intermediate follower reachability fronts (dotted curves) in the double-gyre flow: The time-optimal trajectory of the leader $\mathbf{X}_L^\star(t;\mathbf{y}^s,0)$ is depicted by the solid curve. The starting locations of the followers, $(\mathbf{y}_1^s,\mathbf{y}_2^s)$, are indicated as unshaded round markers. The optimized intermediate follower end points $(\mathbf{y}_1^i,\mathbf{y}_2^i)$, $i=1,2,3$ are represented by unshaded star markers. The depiction of the flow-field is as in Fig. 5.

(forward level-set evolution). Open boundary conditions are implemented on all the walls for (3).

The flow Eqs. (23) are solved using a modular Finite Volume framework (Ueckermann and Lermusiaux, 2011). The framework uses a uniform, two-dimensional staggered C-grid for the spatial discretization. The diffusion operator is discretized using second order central fluxes. The advection operator is discretized using a Total Variation Diminishing (TVD) scheme with the monotonized central (MC) limiter (Van Leer, 1977). The time discretization uses a first-order accurate, semi-implicit projection method, where the diffusion and pressure terms are treated implicitly, and the advection is treated explicitly (Ueckermann et al., 2013). In Fig. 5, we show a few snapshots of the computed flow-field, overlaid on a color plot of the flow magnitude at different non-dimensional times. This flow is now used to illustrate the methodology for formation control with groups of three and four vehicles. We first discuss the case of three vehicles.

The group leader is released from coordinates (0.2, 0.2), shown as a filled circle in the panels of Fig. 5. It is to be steered to the end point (0.8, 0.8) in minimum time. The starting locations of the two follower vehicles are shown as unshaded round markers. The initial positions of the vehicles form an equilateral triangle of side length 0.05. The maximum relative speed of the vehicles is $F=20$. The goal is to steer the group of vehicles in a coordinated fashion such that during their journey: (i) the group leader reaches its end point in minimum time; (ii) the vehicles maintain an equilateral triangle formation as close as theoretically possible; and (iii) the distance between any two vehicles does not exceed $d_{\max}=0.15$.

As a first step, the formation control algorithm determines the time-optimal trajectory of the leader vehicle (Step 1 of Algorithm 1). Fig. 5 shows the evolution of the reachability front of the leader, obtained by solving (3), using numerical schemes described in Appendix A. The front is evolved until it reaches the end point (panel 3). Backtracking (8) is then performed to determine the minimum time trajectory of the leader, depicted as a solid curve in the panels of Fig. 6.

The follower trajectories are determined using steps 4–9 of Algorithm 1. The travel time of the leader, which in this case is equal to $T_L^\star(\mathbf{y}^f)=0.044$, is divided into $N=3$ equal intervals. The location of the leader at the end of the first interval $i=1$ is shown as a square marker in the first panel of Fig. 6. For each follower, (3) is then solved for this interval. Next, a contour extraction algorithm computes the followers' intermediate reachability fronts $(\partial\mathcal{R}_1,\partial\mathcal{R}_2)$, which are depicted as dashed curves. They are used to perform a search of intermediate follower end points that minimize the coordination function (13). Here, we use $\lambda^{\text{side}}=1$, $\lambda^{\text{side}}=0$. The resulting optimized intermediate end points are shown as star markers. From these, backtracking is performed to compute the segments of the follower trajectories. This process is repeated $N=3$ times, evolving follower reachability fronts starting from previously computed intermediate end points. The followers' intermediate end points at the end intervals 2 and 3 are shown in the corresponding panels of Fig. 6.

The time-evolution of all three vehicle trajectories, and the resultant formation are depicted in Fig. 7. The corresponding time-series of the coordination function $\gamma(t)$ is represented as a red curve in Fig. 9a. Its time-averaged value, $\bar{\gamma}$, is found to be 0.320. As evident from Fig. 9a, this large value is due to two periods around times 0.008 and 0.035, where the pattern is distorted. This is also visible on panels b and d of Fig. 7, where a crossover of trajectories occurs, indicating a switch in the orientation of the pattern.

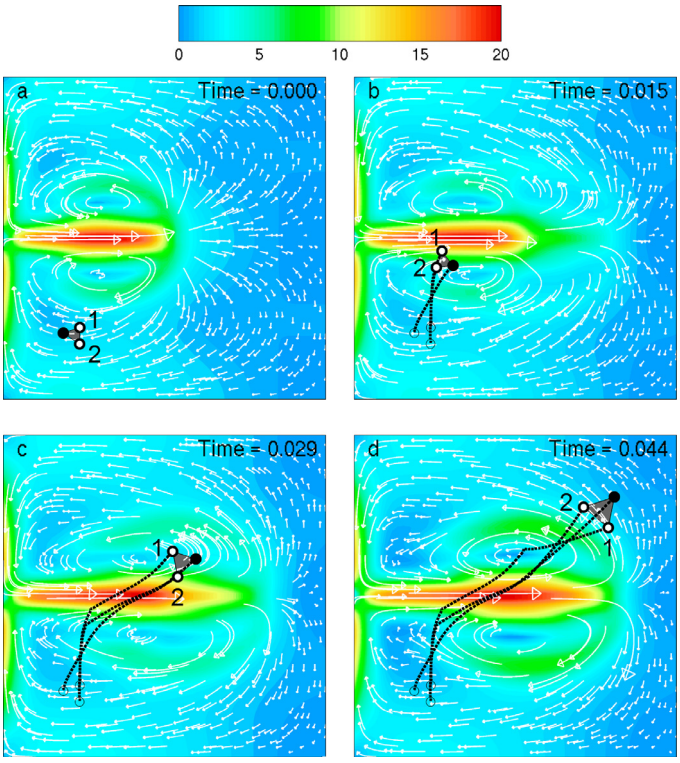

Fig. 7. Dynamic coordination in the double-gyre flow: Time-evolution of trajectories of three vehicles that maintain an equilateral triangle formation. The position of the leader is indicated by a shaded round marker and the two followers are numbered. The depiction of the flow-field is as in Fig. 5.

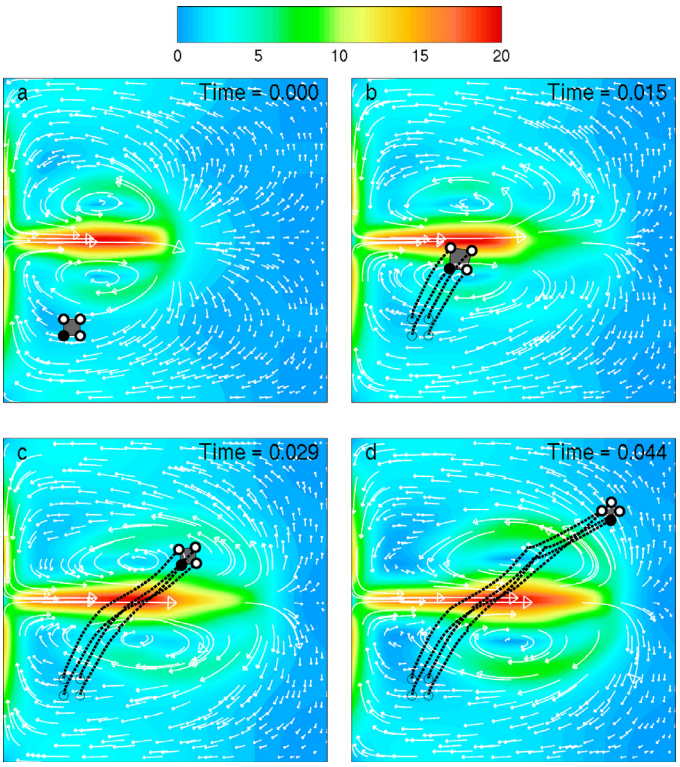

Fig. 8. Dynamic coordination in the double-gyre flow: As Fig. 7, but for the time-evolution of trajectories of four vehicles that maintain a square formation.

The above experiment is now repeated for a group of four vehicles operating in the double-gyre flow. The leader's start point ($\mathbf{y}^s$), the maximum relative speed (F), the allowable distance between the vehicles ($d_{\max}$) and the number of pattern optimizations (N) are kept the same as before. The values of the tuning parameters used in this example are $\lambda^{\text{side}} = 1$, $\lambda^{\text{side}} = 0.5$. The release locations of the followers are depicted by unshaded round markers in Fig. 8a. The remaining panels of Fig. 8 depict the evolution of all the four vehicle trajectories and their resulting formation. We observe that even in this case, the vehicles adequately maintain the required square pattern, successfully adapting the formation size and orientation to gradients in the flow and the leader's trajectory.

The effect of increasing N is now illustrated for both the triangle and square formations. In Fig. 9a, the blue and black curves depict the time-series of γ for $N = 11$ and $N = 15$ respectively for the triangle formation. The value of $\bar{\gamma}$ for $N = 11$ is 0.102 and that for $N = 15$ is 0.061. Therefore, the average coordination function (that indicates the quality of the formation) monotonically decreases as N is increased. Furthermore, it can be seen that for $N = 15$, γ remains less than 0.1 for the entire journey. This trend of monotonic reduction in $\bar{\gamma}$ upon increasing N holds even for the square formation. Fig. 9b depicts the

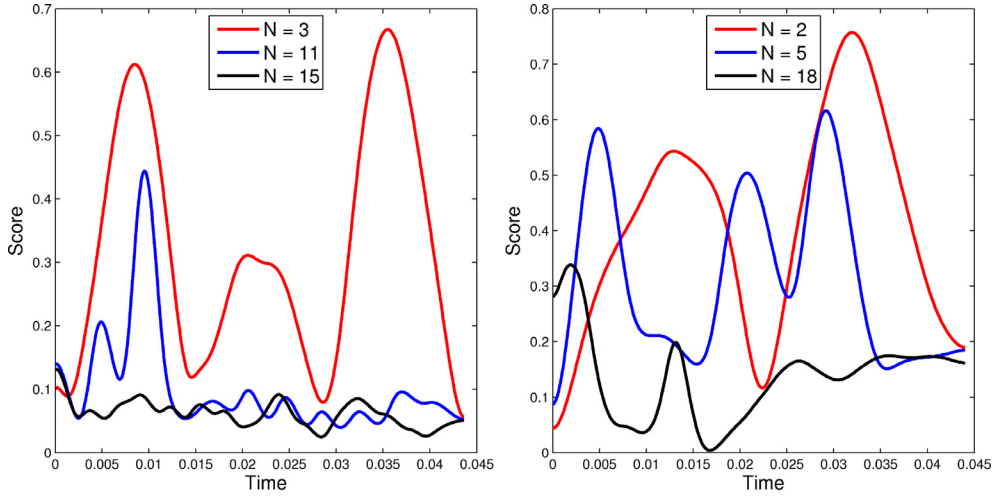

(a) Triangle formation (b) Square formation

Fig. 9. Time-series of the non-dimensional coordination function $\boldsymbol{\gamma}$: This figure shows the effect of increasing N on this γ. As indicated, $\bar{\gamma}$ (the time-averaged value of γ) uniformly decreases as N is increased (note that the triangle and square score functions differ, hence their different numerical values). (For interpretation of the references to color in this figure, the reader is referred to the web version of this article.)

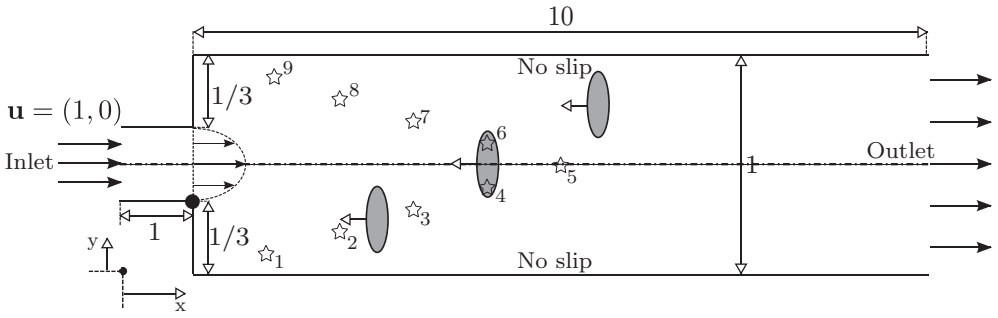

Fig. 10. Schematic of the setup for the flow exiting an idealized strait with dynamic obstacles: Nine vehicles are released from the location $(x = 1, y = \frac{1}{3})$, represented by a round marker. Their respective end points are numbered and indicated by star shaped markers. The three westward bound obstacles are depicted as shaded ellipses (not shown to scale) .

time-series of γ for different values of N for the square formation. As evident from this figure, increasing N lowers $\bar{\gamma}$, thereby uniformly improving the formation quality. These tests therefore confirm that the required formations can be adequately maintained if N is sufficiently large.

5.2. Path planning in the presence of dynamic obstacles in a flow exiting a strait

We now consider the effects of moving obstacles in dynamic flows, specifically, a barotropic jet (2D flow in the horizontal plane) exiting a narrow strait (or estuary) (Cherdron et al., 1978; Durst et al., 1974; Fearn et al., 1990). The strait is assumed to be narrow enough for the Coriolis effects to be negligible. Such flows generally lead to meanders and vortices as the jet exits the constriction. Next, we describe the setup, then outline the schemes used to solve the governing equations, and finally, discuss the results of our path planning.

5.2.1. Setup

Fig. 10 depicts a schematic of the simulation setup. A uniform horizontal flow of speed $U = 1$ (non-dimensional) enters a narrow conduit of width $h = \frac{1}{3}$ at the far left end of the domain. It first fully develops into a steady, symmetric, parabolic flow, reaching the maximum velocity $U_{\max} = 1.5$ at the line of symmetry. At $x = 1$, the flow reaches the abrupt expansion into a channel of larger width, $H = 1$. Eddies form and the flow exits the channel at the right end of the domain, $L = 10$ units downstream of the expansion.

The flow regime largely depends on the Reynolds number (Re). At large enough Re, the flow downstream of the expansion exhibits vortex shedding, which can be either steady or unsteady. Here, we use $Re = 250$. At this Re, we expect the symmetric inlet flow to develop recirculation zones and break to one side of the centerline, depending on the initial perturbations. In order to facilitate this breakage, we introduce a small initial perturbation on the flow in the narrow conduit region.

The control problem is to compute the minimum-time trajectories of nine vehicles in this flow, avoiding three moving forbidden regions in the process. Specifically, the vehicles are all released at the mouth of the expansion from location $(x = 1, y = \frac{1}{3})$ and must be steered downstream, to their respective end points. These numbered star points are located at coordinates $(x = 1, y = \{0.1, 0.9\})$, $(x = 2, y = \{0.2, 0.8\})$, $(x = 3, y = \{0.3, 0.7\})$, $(x = 4, y = \{0.3, 0.7\})$ and $(x = 5, y = 0.5)$. The vehicles have a maximum relative speed of $F = 0.2$ and are released at time $t_s = 6$. The vehicles must avoid passing through three moving circular obstacles of radius 0.15, depicted as shaded ellipses in Fig. 10. The three obstacles are initially centered at *top*: $(x = 6.5, y = 0.75)$, *middle*: $(x = 5, y = 0.5)$ and *bottom*: $(x = 3.5, y = 0.25)$ and move horizontally to the left at constant speeds of 0.85, 0.88 and 0.75 respectively.

5.2.2. Numerics

The geometry is discretized on a uniform, two-dimensional structured grid of 660×60 cells in the x and y directions respectively. The unsteady flow-field is computed using the same equations and numerical schemes as in Section 5.1. A time step of 2×10^{-3} is chosen, to satisfy the Courant–Friedrichs–Lewy (CFL) criterion. Furthermore, as shown in Fig. 10, we assume no-slip boundary conditions at all solid boundaries. A uniform horizontal speed of 1 is imposed across the inlet opening. Open boundary conditions are enforced at the outlet.

The reachability fronts are computed by solving (9), using Appendix A. A time-step of 5×10^{-4} is employed and the spatial discretization is as that used to generate the unsteady flow. To handle the obstacles, at the beginning of each time-marching step, grid cells that lie inside the obstacles are identified. For such cells, (i) F is set to zero, and (ii) the flow-field $\mathbf{V}(\mathbf{x}, t)$ is set to be equal to $\mathbf{V}_\Psi(\mathbf{x}, t)$, the velocity of the corresponding obstacle they lie in. As discussed in Section 3, this step ensures that the reachability front does not pass through the obstacles. At the end, the time-optimal trajectories are computed by backtracking (8).

5.2.3. Results and discussion

The currents and obstacles at different times are shown in panels (1–4)a of Fig. 11. All figures depict streamlines of the flow (in white) overlaid on a color plot of the flow magnitude. The initial flow perturbation leads to counter-rotating eddies on either side of the unstable jet.

The dotted lines shown in panels (1–4)b are time-optimal trajectories, but ignoring the moving obstacles. The strong correlations between flow streamlines and vehicle trajectories clearly show that vehicles utilize the flow to minimize their travel time. All vehicles initially head southward, and then change their direction, moving with the flow. Next, some vehicles branch off from the rest, riding adjoining eddies to reach their respective end points. The vehicle heading to end point 9 exhibits a peculiar behavior. It separates from the main flow, rides a counter-clockwise eddy to head southwest before heading north toward its target. Vehicle 5 rides along the main flow and its meanders all the way to the end of its journey. Unsurprisingly, vehicles 2–9 pass through at least one obstacle along their way, rendering their respective trajectories unsafe. On the other hand, vehicle 1 reaches its end point before encountering any obstacle.

The solid curves in panels (1–4)b represent the trajectories obtained by taking the obstacles into account. It is clear that none of the nine vehicles passes through any of the obstacles. Since vehicle 1 does not encounter any obstacle during its journey (see panel 1b), its trajectory should be unaffected when obstacles are taken into account. This is readily verified from panel 4b, since the solid and dotted trajectories coincide until the end. Panels (1–2)b show that the other eight trajectories initially overlap into two different groups and pass through either side of the bottom obstacle. The northern group consists of two vehicles, heading to end points 8 and 9. After avoiding the bottom obstacle, they turn northward and proceed toward their respective end points, steering clear of the middle obstacle and utilizing favorable eddies. Vehicles 2 and 3 split from the southern group

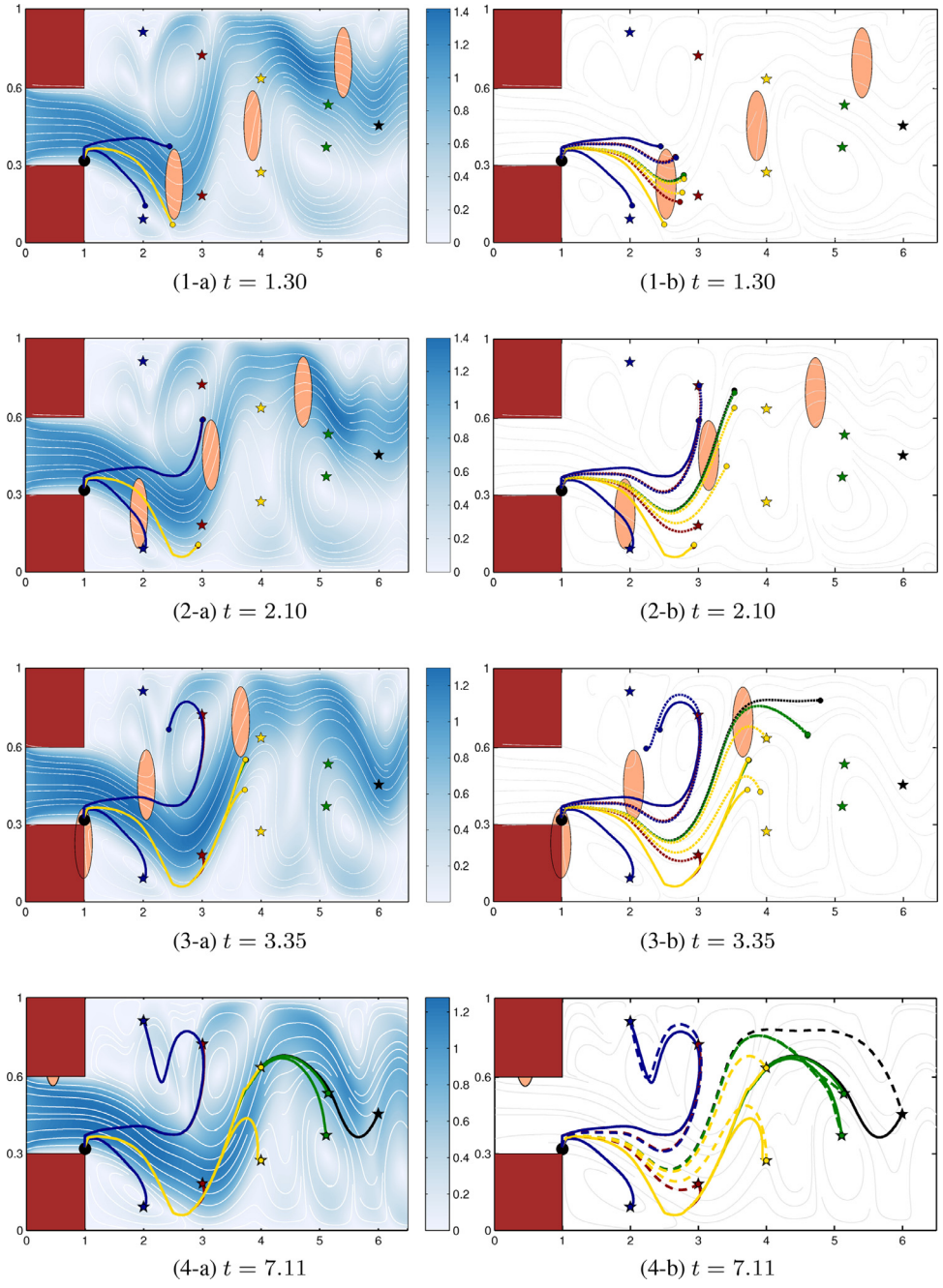

Fig. 11. Dynamic obstacle avoidance in a flow exiting an idealized strait: Time-evolution of the nine optimal vehicle trajectories (colored according to their corresponding end point) is shown in panels 1 through 4. Panels 1–4(a) depict the trajectories computed by accounting for the obstacles (i.e. Eq. (9)). Also shown are streamlines of the flow, overlaid on a color plot of the flow magnitude. For visual clarity, these trajectories are also depicted in panels 1–4(b), but without the colored flow background. The trajectories computed by ignoring the moving obstacles (i.e. Eq. (3)) are shown as dashed curves in panels 1–4(b). (For interpretation of the references to color in this figure legend, the reader is referred to the web version of this article.)

as it moves north-east with the main flow. The remaining members brush the boundary of the top obstacle before dispersing toward their respective end points. As a result, all the computed paths optimally avoid the dynamic obstacles. Therefore, this study conclusively verifies our methodology for time-optimal path planning in the presence of dynamic obstacles.

5.3. Formation control and dynamic obstacle avoidance in the Philippines

We now study vehicle coordination and dynamic obstacle avoidance in the multi-scale flows of the Philippine Archipelago. The Philippine Archipelago is chosen because of its complex geometry, with numerous islands, passages and seas (see Fig. 12). The multi-scale dynamics, driven by open ocean and atmospheric forcing, various currents, eddies and tides provide a challenging environment for path planning.

5.3.1. Multiresolution ocean modeling and data-assimilative simulations

To predict the ocean dynamics in the Philippine Archipelago region, we employ the MIT Multidisciplinary Simulation, Estimation, and Assimilation Systems (MSEAS) (Haley and Lermusiaux, 2010; MSEAS Group, 2010). MSEAS has been used for fundamental research and for realistic tidal-to-mesoscale simulations and predictions in

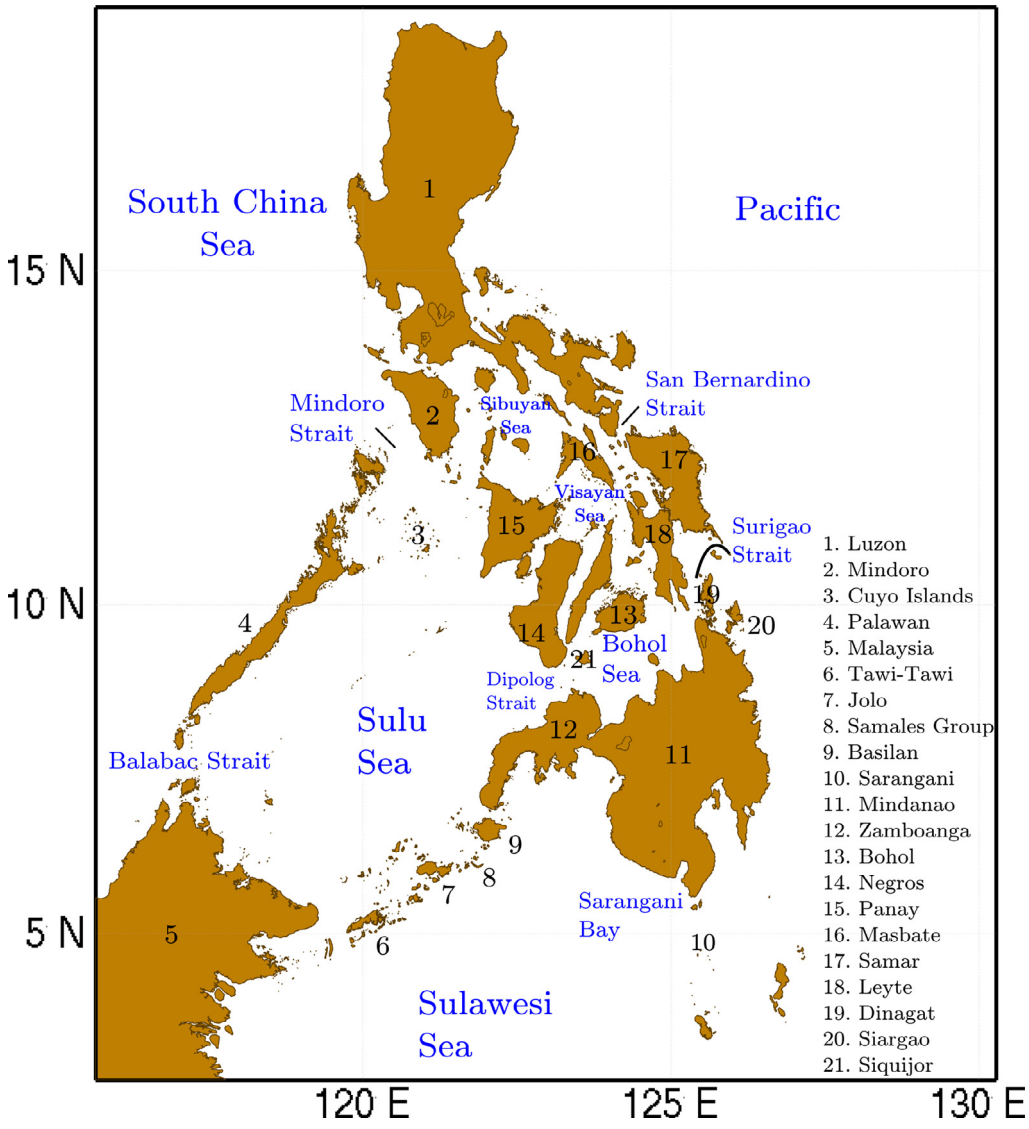

Fig. 12. The Philippine domain: Major islands indexed in black; water bodies in blue. (For interpretation of the references to color in this figure legend, the reader is referred to the web version of this article.)

varied regions of the world's ocean (Colin et al., 2013; Gangopadhyay et al., 2011; Haley et al., 2009; Leslie et al., 2008; Onken et al., 2008; Ramp et al., 2011), including monitoring (Lermusiaux et al., 2007), real-time ecosystem and acoustic predictions (Beşiktepe et al., 2003; Xu et al., 2008) and environmental management (Cossarini et al., 2009).

The present MSEAS ocean field estimates are data-assimilative re-analyses for February 5–March 24, 2009, as part of the Philippine Straits Dynamics Experiment (PhilEx; Gordon and Villanoy, 2011). The multiresolution simulations (Lermusiaux et al., 2011) solve the hydrostatic primitive-equations with a nonlinear free surface, using second-order structured finite volumes and a set of telescoping domains interconnected by implicit two-way nesting (Haley and Lermusiaux, 2010). The domains have 9 km, 3 km and 1 km horizontal resolutions and 70 optimized vertical levels. The simulations are initialized using the February NODC World Ocean Atlas 2005 (WOA05) climatology mapped with the fast-marching-method-based objective analysis (Agarwal and Lermusiaux, 2011). Initial velocities are obtained solving an optimization problem (Haley et al., 2015), combining: geostrophic balance; velocity anomalies derived from sea surface height anomaly (CCAR; Leben et al., 2002); feature model velocities for the South China Sea and the bottom currents through the Mindoro and Dipolog Straits; and, open boundary transports from the HYbrid Coordinate Ocean Model (HYCOM; Bleck, 2002; Hurlburt et al., 2011). The simulations were forced with atmospheric fluxes from the Coupled Ocean/Atmosphere Mesoscale Prediction System (COAMPS; Hodur, 1997) and barotropic tides created using (Logoutov and Lermusiaux, 2008) with boundary forcing from OTIS (Egbert and Erofeeva, 2002). Additional information on these simulations is provided in Lermusiaux et al. (2011).

5.3.2. *Currents forcing underwater vehicles*

The MSEAS re-analysis currents force the simulated underwater vehicles. We assume that all AUVs follow a yo-yo (saw-tooth) pattern in the vertical. The yo-yo pattern is chosen because it is the innate glider motion and also commonly utilized to collect in situ data by AUVs, e.g. Rudnick et al. (2004), Schofield et al. (2010), Gawarkiewicz et al. (2011), and Høydalsvik et al. (2013). To sample the thermocline in the region, we employ yo-yo patterns from the near surface to either the local near bottom or 400 m depth, whichever is shallower. We also assume that the vertical ocean speeds (which are relatively small) have limited effects on the AUV motions and that the time scales of variability in the horizontal currents are longer than the time needed to complete a single vertical excursion (the time-scales of vertical motion are much smaller than those of the horizontal motion). Under these assumptions, the total horizontal drift of

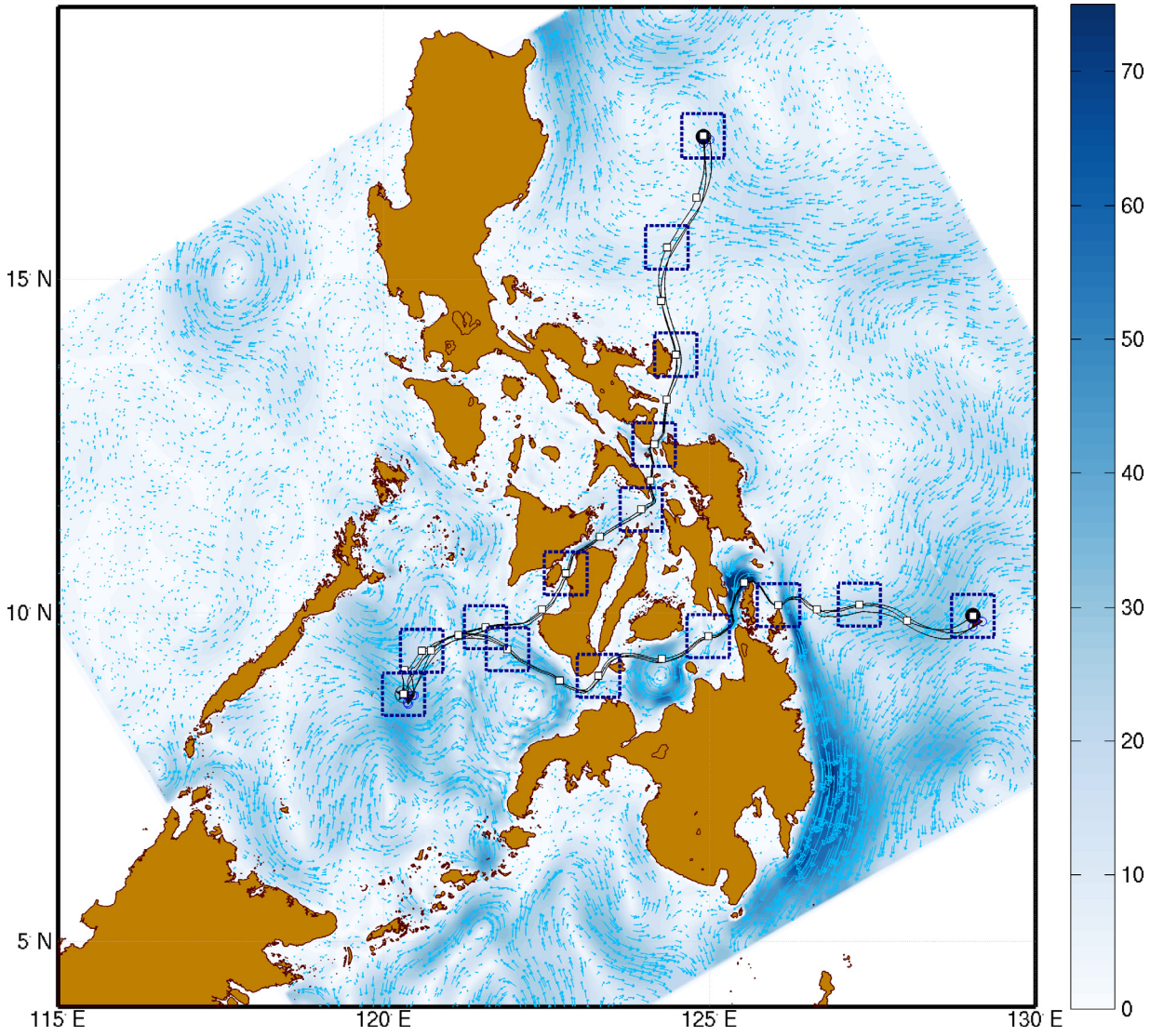

Fig. 13. Dynamic coordination in the Philippines: Final minimum-time trajectories of two groups of vehicles that maintain an equilateral triangle formation. The trajectories are superimposed on the vertically-averaged flow-field of horizontal currents on 16 March 2009 (i.e. 38 days after the deployment). Flow patterns are indicated by curved vectors, overlaid on a color plot of the flow magnitude (colorbar units: cm/s). The panels of Figs. 14 and 15 depict magnified views of the regions indicated by dotted squares. (For interpretation of the references to color in this figure legend, the reader is referred to the web version of this article.)

vehicles is that produced by the vertically averaged horizontal currents. In other words, the horizontal currents that a vehicle would encounter during its yo-yo motion would be the horizontal currents integrated along its path, from the near surface to either the local near bottom or 400 m depth. These currents are what facilitate (or impede) their forward motions. What differentiates the vehicles is then simply their own nominal forward horizontal speeds. In the results to follow, the path-planning problem is solved using the 0–400 m vertically-averaged horizontal currents as the flow-field $\mathbf{V}(\mathbf{x}, t)$. For fully 4D path-planning in realistic ocean flows where the AUV motion is 3D and not restricted to vertical yo-yo patterns, we refer to Lermusiaux et al. (2015).

To understand the optimal paths, we briefly summarize the 2D vertically-averaged horizontal Philippine flows (see Lermusiaux et al., 2011; Lolla et al., 2014a for more dynamical studies). In the Pacific Ocean, the large-scale horizontal flow consists of the North Equatorial Current (NEC) and its active eddy field formed as the NEC impinges upon the Archipelago around 14°N (Qu and Lukas, 2003) and then splits into two boundary currents, the equatorward Mindanao current and the northward Kuroshio (see Fig. 13). A portion of the Mindanao current flows along the island of Mindanao into the Sulawesi Sea and finally into the Sulu Sea. The exchanges between the Pacific and the Sulu Sea also occur through the Luzon Strait (outside of the modeling domain) via the South China Sea; through the San Bernardino Strait and the Sibuyan Sea; and through the Surigao Strait, Bohol Sea, and Dipolog Strait. These latter flows are variable and observed in both directions, either into or out of the Sulu Sea (Lermusiaux et al., 2011).

Although tidally very active, the mean flows through the San Bernardino Strait are small (Gordon et al., 2011). The neighboring current systems in the Sibuyan Sea are also variable but relatively weak, and thus will have smaller effects on vehicles entering or leaving the Sulu Sea. Tidal currents are also very strong at the Surigao Strait, but on average, the upper currents show mostly an inflow from the Pacific through Surigao Strait into the Bohol Sea. These currents join up with flows in the Bohol Sea, then continue through Dipolog Strait and into the Sulu Sea (see also Gordon et al., 2011; Hurlburt et al., 2011; Lermusiaux et al., 2011). For most of the time during February 5–March 24, 2009, the Sulu Sea contains a relatively strong cyclonic eddy and a northward current along Negros Island. However, there are also time periods when that current reverses in direction. The Sulu Sea also has a complex and intermittent eddy field. On monthly

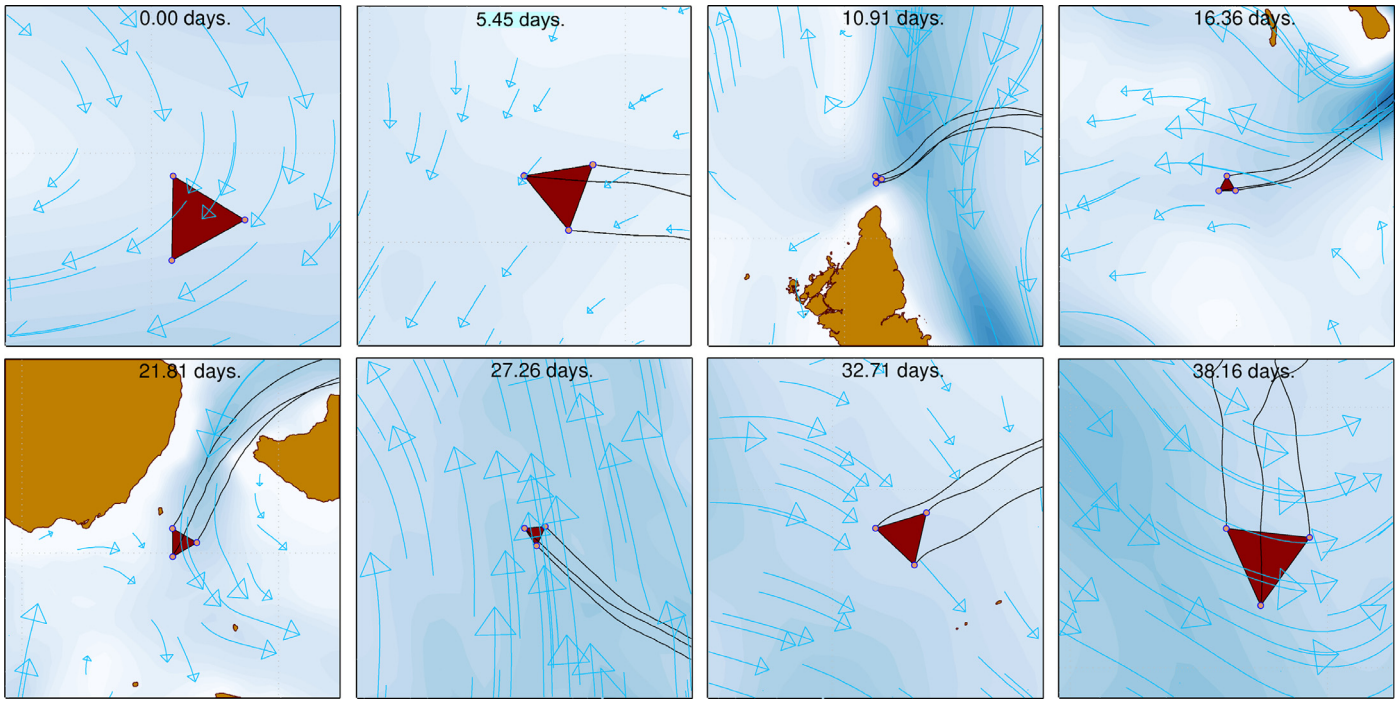

Fig. 14. Coordinated motion of vehicles of the southern group: The above panels provide magnified views of the vehicles of the southern group at different times (indicated at the top of the panels) along their journey. The flow shown in each panel is the local vertically-averaged horizontal flow-field encountered by the vehicles at the corresponding time.

average, it experiences net inflows from Balabac, Mindoro/Panay and Dipolog Straits, and net outflows through the Sibutu Passage and the Sulu Archipelago.

Level-set numerics. Numerical schemes outlined in Appendix A are used to solve Eqs. (3), (9) and (8) in all the results presented next. A spatial discretization of 3 km × 3 km resolution and a time-step of 5 min (chosen to satisfy the CFL condition) are used for the reachability front evolution. Grid cells that lie inside the stationary islands are masked during the solution of Eqs. (3) and (9). Open boundary conditions are imposed on all the domain boundaries. For the numerical integration, space and time are non-dimensionalized by reference values of 3 km and 3h respectively.

5.3.3. Formation control in the Philippines

In Lolla et al. (2014a), we discussed various scenarios of all-to-all broadcast between multiple transmitters and receivers, where the participating vehicles execute their trajectories independent of each other, i.e. without any coordination. Presently, we predict the minimum-time coordinated paths of two groups of vehicles which aim to maintain an equilateral triangle pattern throughout their journeys.

We consider two groups consisting of three vehicles each, released from different locations in the Pacific ocean. The vehicles of the "southern group" are released from (9°57′N, 129°3′ E; 9°47′N, 129°2′ E; 9°52′N, 129°11′ E) and those of the "northern group" from (17°7′N, 124°54′ E; 17°0′N, 124°54′ E; 17°3′N, 125°0′ E). These points lie at the vertices of two equilateral triangles, side lengths 18 km (southern group) and 12 km (northern group). Without loss of generality, the vehicle released at the first of the three coordinates of a group is assigned to be the leader of that group, while the other two are the followers. Leaders of both the groups need to reach a common end point in the Sulu Sea, with coordinates (8°46′N 120°18′ E). The southern group is assumed to be capable of relative speeds of up to 27 cm/s, while the northern group has a maximum relative speed of 54 cm/s. The goal is to predict minimum-time trajectories of both groups between their start and end points, requiring them to maintain respective equilateral triangle patterns during their journey. Furthermore, the distance between any two vehicles of each group cannot exceed $d_{\max} = 20$ km. As in Section 5.1, we use $\lambda^{\text{side}} = 1$ and $\lambda^{\text{angle}} = 0$ for the score function γ.

Using Step 1 of the formation control algorithm, the minimum travel times of the group leaders are first computed. The southern group leader reaches the end point in $T^{\star}_{L,S} = 38.5$ days. Its northern counterpart requires only $T^{\star}_{L,N} = 23.4$ days due to its higher speed. Their time-optimal trajectories are then calculated by solving the backtracking equation (8). Next, the overall journey durations of each group leader, $[0, T^{\star}_{L,S})$ and $[0, T^{\star}_{L,N})$, are divided into $N = 15$ intervals of equal length. Trajectories of both pairs of followers are then formed as unions of their respective intermediate segments spanning these intervals. To calculate the intermediate follower trajectory segments (lines 5–7 of Algorithm 1), follower reachability fronts are evolved (line 5) over the duration of each interval. Intermediate end points are then computed (line 6) by performing the pattern optimization (17). Finally, backtracking (line 7) yields the trajectory segments.

Fig. 13 depicts the trajectories of both groups of vehicles overlaid on a map of the Philippines. Also shown is the flow-field at the end of 38.5 days, colored by magnitude. A magnified view of both groups of vehicles and the pattern they maintain is provided in the panels of Figs. 14 and 15. These magnified views correspond to locations in Fig. 13 marked by squares. Positions of the group leaders at the intermediate pattern optimization points are shown as unshaded square markers.

Vehicles in the northern group enter the Visayan Sea through the San Bernardino Strait, skirting the Masbate Island along the way. They pass through the strait between Panay and Negros Islands to reach the Sulu Sea. Then, they utilize favorable counter-clockwise currents in the Sulu to reach their end points. Vehicles of the southern group ride along the large-scale Pacific currents, go around the northern edges of Siargao and Dinagat Islands, into the Surigao Strait. There, they encounter strong intermittent tidal flows as they enter the Bohol Sea. On their way out of Bohol Sea, they pass between Negros and Siquijor Islands. Once they enter the Sulu Sea, they utilize favorable counter-clockwise currents to reach their end points, in a manner similar to vehicles from the northern group.

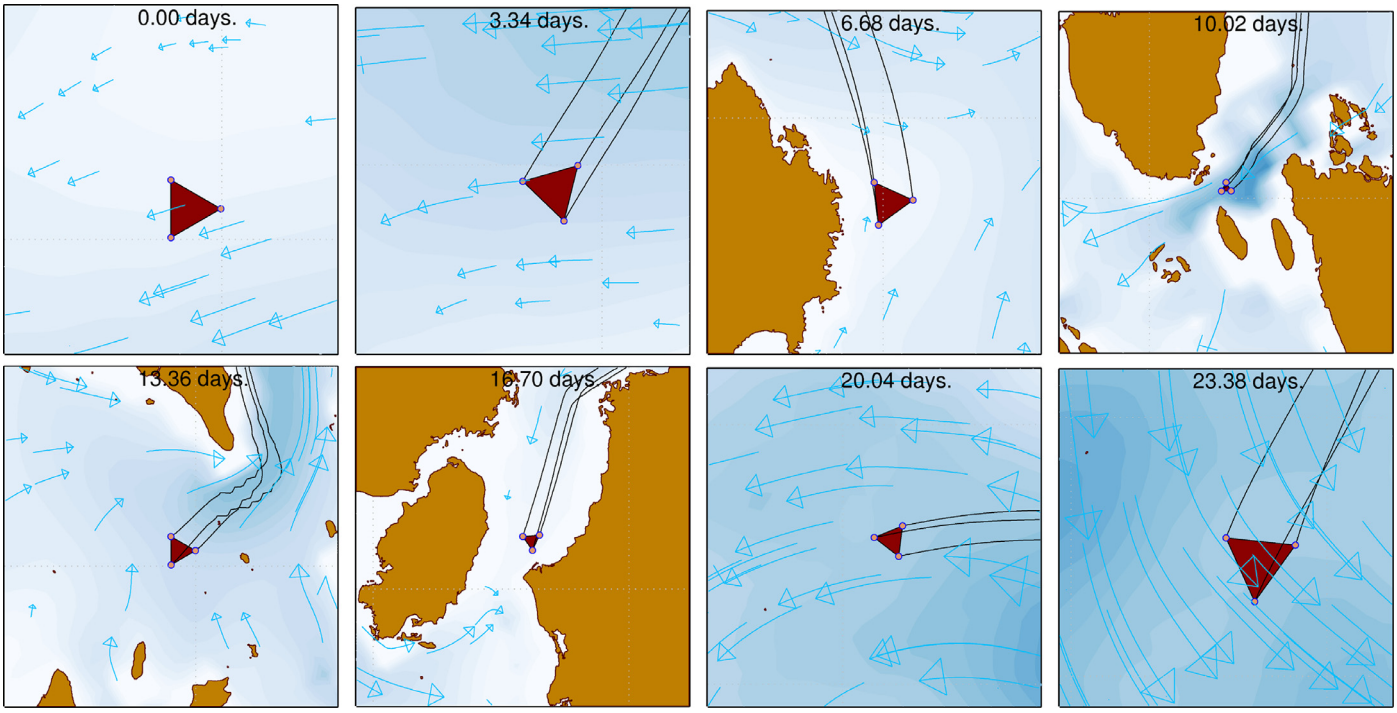

Fig. 15. Coordinated motion of vehicles of the northern group: The above panels provide magnified views of the vehicles of the northern group at different times (indicated at the top of the panels) along their journey. The flow shown in each panel is the local vertically-averaged horizontal flow-field encountered by the vehicles at the corresponding time.

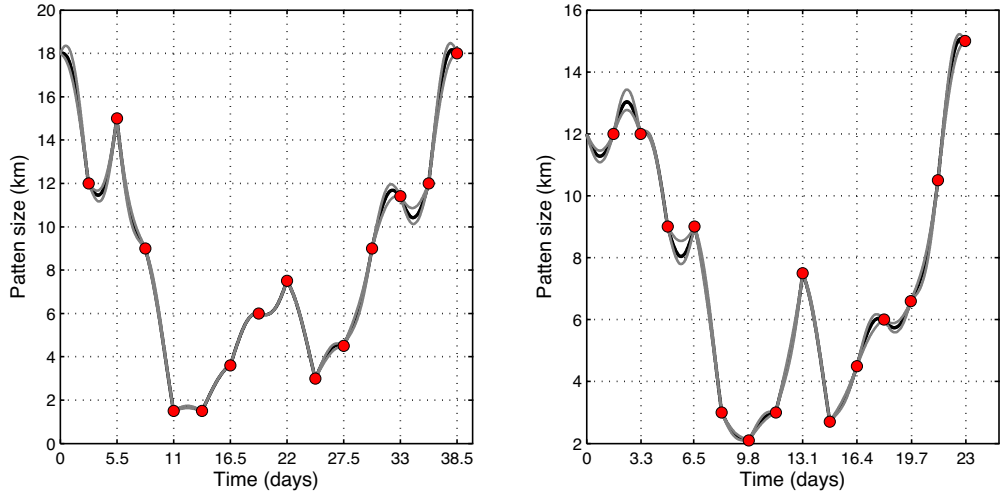

Fig. 16. Time-series of the size of the triangle formed by vehicles of each group: The black curve represents the average side length of the triangle. The upper and lower gray curves represent the maximum and minimum side lengths respectively. The shaded round markers indicate the times at which each *pattern optimization* procedure is carried out.

Fig. 16 shows the variation in size of the triangle formed by vehicles of both groups of vehicles, plotted against their respective travel times. The black curve indicates the average side length of the triangle, while the grey curves depict the maximum and minimum side lengths. Red markers indicate the times when pattern optimizations are performed (Eq. (17)). We see that our methodology for coordinated pattern formation maintains the equilateral triangle well, since the grey curves almost overlap with the black ones throughout the duration of both missions. It is also interesting to note that the average triangle size reduces as the vehicles pass through the Archipelago, especially through the narrow straits with strong tides, and then increases once they reach the Sulu Sea. In all cases, the maximum distance between the vehicles does not exceed the limit of 20 km, as required. Fig. 17 shows how the coordination function γ varies with time for each group. We see that γ never exceeds 0.07 for either group. Moreover, we see that γ has a local minima at the pattern optimization times. This is because the formation is monitored only at these times, and the vehicles may deviate from the required geometry at other times. As shown in Section 5.1, as N increases, so will the quality of the pattern throughout the journey (results with smaller N are not shown here since they are similar to these of the double-gyre examples). Overall, this example illustrates that our new coordinated formation control is applicable to realistic complex ocean flows and island geometries.

5.3.4. *Path planning in the presence of dynamic obstacles in the Philippines*

We now study our time-optimal path planning with dynamic obstacle avoidance using the Philippines region as a test-bed. An

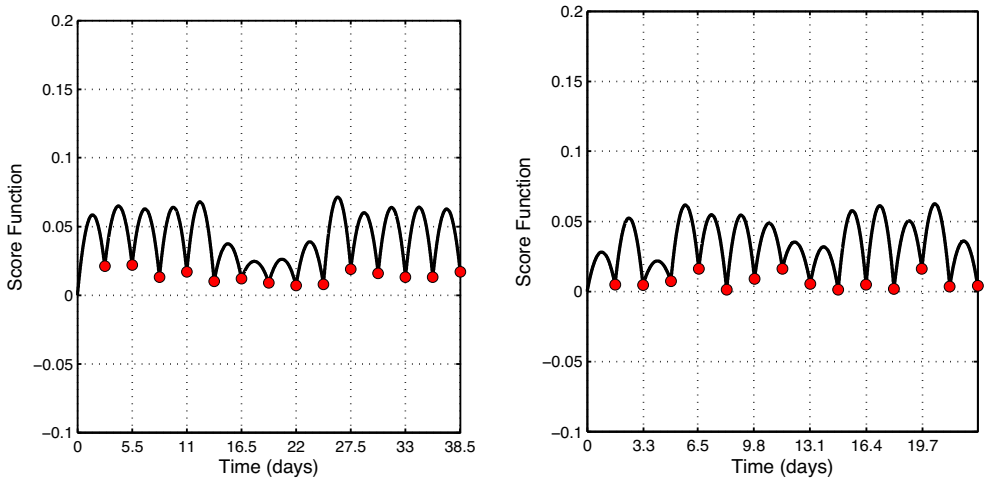

Fig. 17. Time-series of the coordination function for both groups of vehicles: The shaded round markers indicate the times at which each *pattern optimization* procedure is carried out.

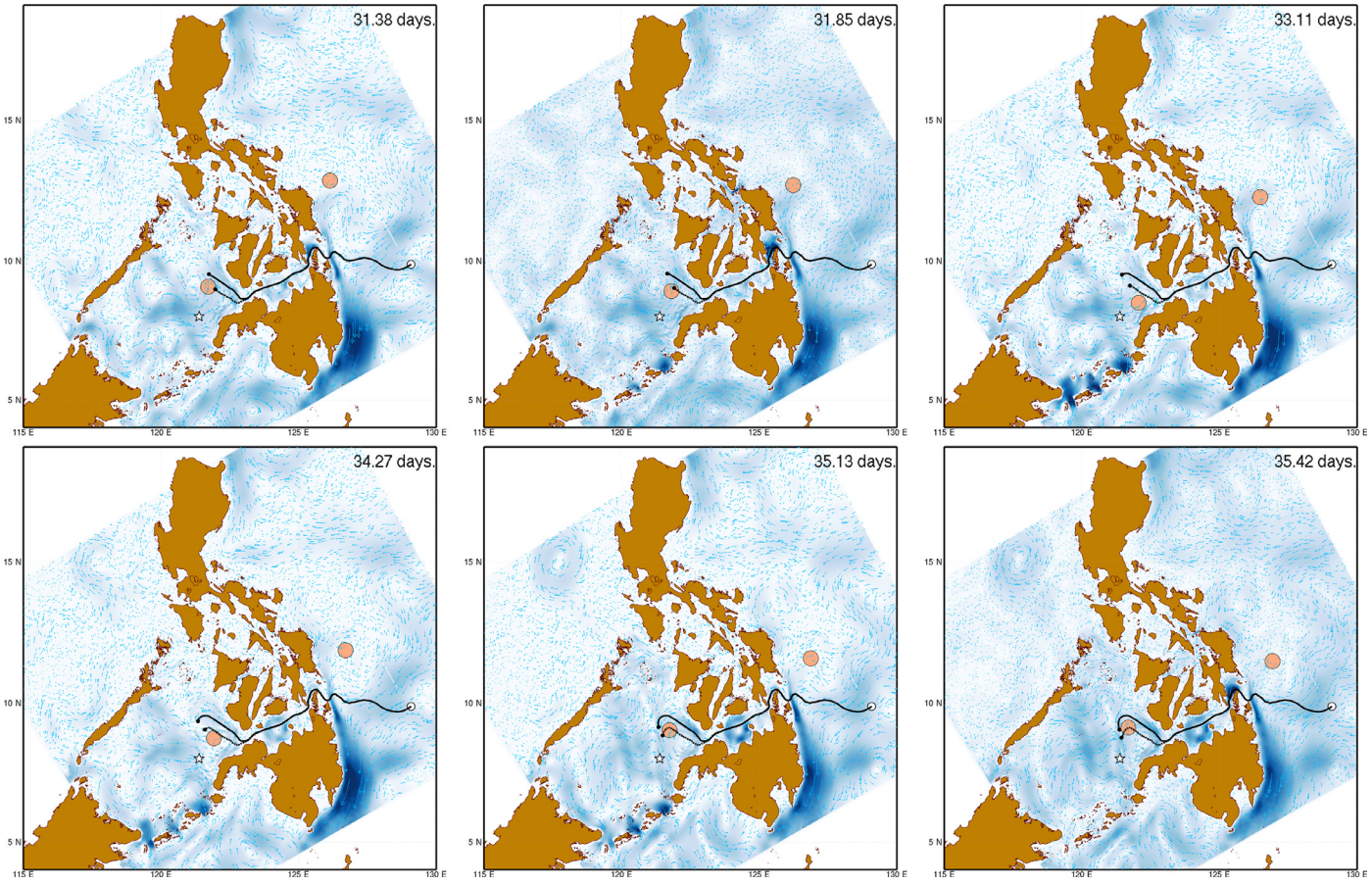

Fig. 18. Dynamic obstacle avoidance in the Philippines: The start and end points of the glider are indicated by unshaded round and star shaped markers, respectively. The two dynamic obstacles are shown as shaded circles. The solid black curve is the time-optimal trajectory that avoids them; the dotted black curve is the optimal trajectory that ignores them. The flow shown in each panel is the vertically-averaged horizontal flow-field at the corresponding time elapsed after vehicle deployment, indicated at the top of the panel.

underwater glider, which can travel at a maximum relative speed of $F = 25$ cm/s is deployed from the Pacific at (9°54′N, 129°5′ E). The glider must arrive, in minimum time, at a pick-up location with coordinates (7°46′N, 121°32′ E) in the Sulu Sea. The locations of the start (round marker) and end point (star marker) are shown in the panels of Fig. 18. Two dynamic forbidden regions of radius 30 km, depicted as round shaded areas in Fig. 18, are also simulated. They move back and forth between two fixed locations at an absolute speed of 50 cm/s. The first operates between (9°23′N, 128°8′ E) and (13°37′N, 125°42′ E) in the Pacific and the second between (10°17′N, 120°59′ E) and (8°26′N, 122°6′ E). Each of these moving obstacles is initially located at its highest latitude. The goal is to predict the minimum-time path of the glider, accounting for the two moving obstacles and the stationary islands.

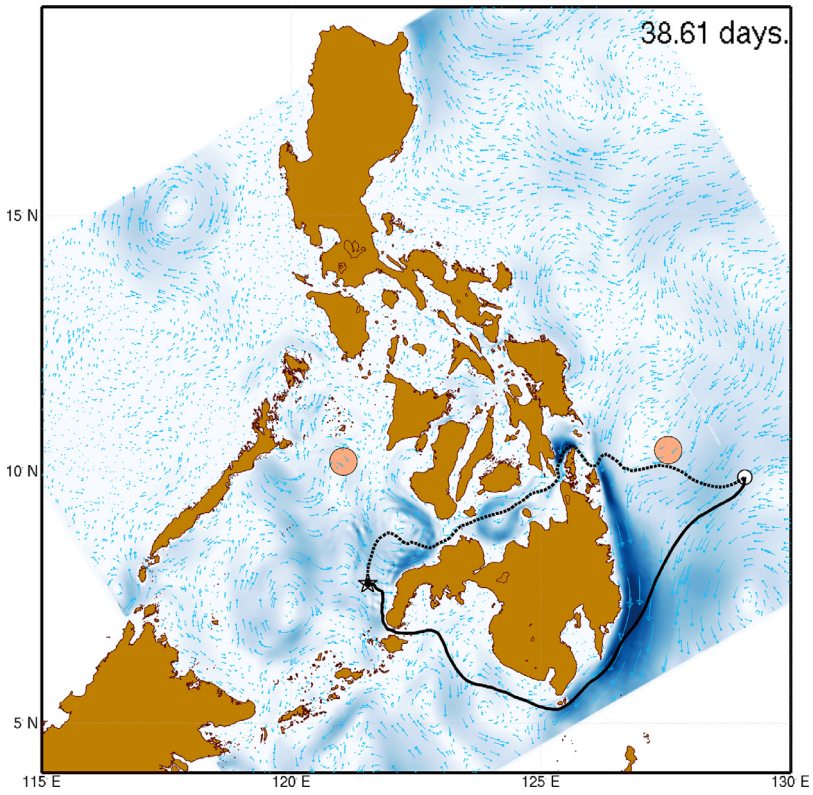

Fig. 19. Dynamic obstacle avoidance in the Philippines—sensitivity of the optimal trajectory: Time-optimal trajectories of a vehicle operating between given a start (round marker) and end point (star shaped marker). The two dynamic obstacles are shown as shaded circles, at their position at the final time. The dotted black curve represents the time-optimal trajectory computed by ignoring the obstacles and the solid black curve is determined by accounting for them.

Fig. 18 shows the time-optimal trajectories of two gliders, one computed by ignoring (dotted curve) the dynamic obstacles and the other computed by accounting for them (solid curve). We note that both these trajectories coincide until they enter the Sulu Sea through the Bohol Sea. This indicates that the obstacle in the Pacific has no effect on the optimal trajectory. This is because by the time it intercepts the trajectories, both the gliders have already entered the Bohol Sea through the Surigao Strait. Therefore, for its present speed and operating location, the obstacle in the Pacific has no bearing on the time-optimal trajectory of the glider. The solid and the dotted trajectories split upon exiting the Bohol Sea, due to the moving obstacle in the Sulu Sea. We observe that the glider corresponding to the dotted trajectory passes through the obstacle shortly after 31.38 days of deployment. During this time, both the gliders move north-west toward the Palawan islands due to the strong anti-clockwise current they face upon entering the Sulu Sea. After unfavorable current recedes, both the gliders turn toward their common end point. After roughly 35.13 days, the dotted trajectory again passes through the obstacle, while the solid trajectory correctly avoids the obstacle by skirting around its west. Therefore, the glider corresponding to the solid trajectory does not pass through either of the moving obstacles on its way to the end point. This shows that our methodology correctly accounts for the moving obstacles during its time-optimal path planning.

The presence of dynamic obstacles in the environment can significantly alter the time-optimal trajectory of the glider. We now change the location of the end point to (8°0′N, 121°23′ E), keeping the rest of the problem parameters the same. The optimal trajectories in this case are depicted in Fig. 19. We observe that the trajectory that ignores the obstacles (dotted curve) reaches the end point through the Surigao Strait and the Bohol Sea. However, the trajectory that accounts for the obstacles (solid curve) rides the Mindanao current and enters the Sulu Sea through the passage between the Basilan Island and the Zamboanga Island.

6. Summary and conclusions

For many ocean applications, the coordinated operation of multiple AUVs provides significant advantages such as robustness and efficiency, thereby enhancing the utility of individual vehicles. Most coordination techniques usefully assume that the kinematics of vehicles are unaffected by the benign environment in which they operate. However, in the ocean, longer-range underwater vehicles, especially gliders, possess limited relative operating speeds. It is thus important to account for the currents while planning their optimal trajectories. This paper first derived a novel methodology for distance-based coordination among underwater vehicles operating in minimum-time within strong and dynamic flows. The methodology rigorously integrates ocean modeling with our recent level-set approach for time-optimal path planning (Lolla et al., 2014b) and an efficient optimization for coordinated motions. The key idea is to continuously compute the next time-optimal reachable locations and to select among these time-optimal locations the short-term end points and headings that lead to the best coordination. Specifically, the methodology regularly computes the short-term reachability fronts for each vehicles, then selects the best reachable end points by optimizing a *coordination function*, and finally unifies the resulting short-term time-optimal and coordination-optimal trajectories. In practice, ocean model predictions and this optimal control scheme are integrated to efficiently forecast safe, time- and coordination-optimal paths. The resulting optimal heading directions are then provided to the vehicle controller, and updated with new forecasts. This coordination methodology is developed for formation control, where the goal is for a group of vehicles to achieve and maintain a specific

pattern during the course of their minimum-time journey. This time-optimal formation control is exemplified using a new score function that is suitable to maintain any regular polygon formation. Nevertheless, the methodology is generic and the governing principles are applicable to swarms with diverse coordination constraints.

A second contribution of this paper is a non-intrusive technique for time-optimal path planning in the presence of dynamic obstacles and 'forbidden' regions. This technique generalizes our level-set methodology to handle moving obstacles, without any increase in the computational cost. Specifically, inside the moving obstacle, the level-set equation is modified by suppressing the normal motion of the front evolution and replacing the flow velocity with that of the obstacle. This ensures that no portion of the reachability front penetrates through the moving obstacles.

Varied simulations illustrated and evaluated these new methodologies. First, a wind-driven double-gyre flow was used to analyze the dynamic pattern formation for three vehicles in an equilateral triangle shape and four vehicles in a square pattern. The results demonstrate that increasing the frequency of *pattern optimization* operations reduces the computational cost and critically the average *coordination function*, thereby improving the overall quality of the formation. Second, simulations of currents exiting an idealized strait/estuary were utilized to analyze the dynamic obstacle avoidance. The results show that vehicles successfully avoid collision with the moving obstacles. Moreover, the time-optimal trajectories computed using this technique remain unchanged when the corresponding vehicles do not encounter an obstacle during their journey. Finally, both methodologies were applied to the multi-scale ocean flows of the complex Philippine Archipelago. The data-assimilative re-analyses of the MSEAS ocean modeling system were utilized to generate the currents. Results demonstrate that the vehicles successfully avoid the islands and adapt the formation size to the local currents' gradients and variability, and also to the width of the inter-island passages (linked to Remark 8 of Section 4.3 on deadlock scenarios). Vehicles also avoid the moving obstacles in the region, in some cases by significantly altering their time-optimal trajectories.

Future opportunities include extending the methodology for dynamic coordination to other types of formations and geometric patterns, including inter-vehicle communication (Ren and Sorensen, 2008; Sisto and Gu, 2006). Secondly, the schemes presented here can be coupled with techniques for adaptive sampling (Choi and How, 2010; Leonard et al., 2007) and adaptive modeling (Lermusiaux, 2007; Lermusiaux et al., 2007) so as to collect observations that optimally sample ocean fields or best enable model learning, respectively. This requires an integration of stochastic ocean models (Lermusiaux et al., 2006) with data assimilation and control.

Acknowledgments

We acknowledge the Office of Naval Research for supporting this research under grants N00014-09-1-0676 (Science of Autonomy, A-MISSION), N00014-14-1-0476 (LEARNS), N00014-07-1-0473 (PhilEx) and N00014-12-1-0944 (ONR6.2) to the Massachusetts Institute of Technology (MIT). We are thankful to the members of the MSEAS group and to the PhilEx team for several helpful discussions. We also thank the anonymous reviewers for their useful comments.

Appendix A. Numerical schemes

We now summarize the numerical schemes utilized to discretize and solve (3) and (8) (details are in Lolla, 2012). These equations are solved using a Finite Volume framework implemented in MATLAB. The term $|\nabla\phi^o|$ in (3) is discretized using either a first order (Lolla, 2012; Sethian, 1999) or a higher order (Yigit, 2011) upwind scheme and $\mathbf{V}(\mathbf{x}, t)\cdot\nabla\phi^o$ is discretized using a second order TVD scheme on a staggered C-grid (Ueckermann and Lermusiaux, 2011).

A1. Forward level-set evolution

We discretize (3) in time using a fractional step method as follows:

$$\frac{\bar{\phi}-\phi^o(\mathbf{x},t)}{\Delta t/2} = -F|\nabla\phi^o(\mathbf{x},t)|, \tag{A.1}$$

$$\frac{\bar{\bar{\phi}}-\bar{\phi}}{\Delta t} = -\mathbf{V}\left(\mathbf{x}, t+\frac{\Delta t}{2}\right)\cdot\nabla\bar{\phi}, \tag{A.2}$$

$$\frac{\phi^o(\mathbf{x},t+\Delta t)-\bar{\bar{\phi}}}{\Delta t/2} = -F|\nabla\bar{\bar{\phi}}|, \tag{A.3}$$

where (A.1)–(A.3) are solved only in the interior cells of the domain. For boundaries that are open inlets/outlets or side walls (i.e. not interior obstacles nor forbidden regions), a zero normal flux was presently used on ϕ^o, and on the intermediate variables $\bar{\phi}$ and $\bar{\bar{\phi}}$ at each time step. We have also used weaker open conditions such as zero second order derivatives (allows non-zero gradients). In general, more complex open boundary conditions can be used as done in regional ocean modeling (Haley and Lermusiaux, 2010; Lermusiaux, 1997). Stationary obstacles in the domain are masked. For points adjacent to the mask, the necessary spatial gradients are evaluated using neighboring nodes that do not lie under the mask.

The reachability front $\partial\mathcal{R}$ is extracted from the ϕ^o (narrow-band) field at every time step using a contour algorithm. In a 2D problem, the amount of storage required for this is not significant, because $\partial\mathcal{R}$ is a 1D curve which is numerically represented by a finite number of points. We also note that this contour extraction is not needed: we could simply store the times when the zero contour of ϕ^o crosses each grid point in order to compute the normals for the backtracking (Yigit, 2011).

A2. Backtracking

Eq. (8) is discretized using first order (Lolla, 2012) or higher-order (Yigit, 2011) time integration schemes. Ideally, it suffices to solve (3) until the level-set front first reaches $\mathbf{y}^f$. However, due to the discrete time steps, a more convenient stopping criterion is the first time, T, when $\phi^o(\mathbf{y}^f, T) \le 0$. Due to this, $\mathbf{y}^f$ does not lie on the final contour $\partial\mathcal{R}(T;\mathbf{y}^s,t_s)$ exactly. Thus, we first project $\mathbf{y}^f$ onto $\partial\mathcal{R}(T;\mathbf{y}^s,t_s)$. The projected $\hat{\mathbf{n}}_p$ is computed as the unit normal to $\partial\mathcal{R}(T;\mathbf{y}^s,t_s)$ at the projected point. The discretized form of (8),

$$\frac{\mathbf{X}_p^\star(t-\Delta t;\mathbf{y}^s,t^s)-\mathbf{X}_p^\star(t;\mathbf{y}^s,t^s)}{\Delta t} = -\mathbf{V}(\mathbf{X}_p^\star,t) - F\underbrace{\frac{\nabla\phi^o(\mathbf{X}_p^\star,t)}{|\nabla\phi^o(\mathbf{X}_p^\star,t)|}}_{\hat{\mathbf{n}}_p(\mathbf{x},t)}, \tag{A.4}$$

is marched back in time until we reach a point on the first saved contour and this generates a discrete representation of $\mathbf{X}_p^\star(t;\mathbf{y}^s,t^s)$. Along the way, we project each newly computed trajectory point, $\mathbf{X}_p^\star(t-\Delta t;\mathbf{y}^s,t^s)$ onto the corresponding intermediate level-set contour (see Lolla, 2012).

Appendix B. Local formation control with a predictor–corrector scheme

A local control technique based on a first-order predictor–corrector scheme for geometric pattern formation and maintenance, inspired by a virtual structure approach (Swaminathan and Minai, 2005), is described in Lermusiaux et al. (2015); Lolla (2012). In this approach, a virtual *center of mass* (denoted by C) is assigned as a representative of each pattern to be maintained. For each group/swarm, the minimum-time trajectory $\mathbf{X}_C^\star(t;\mathbf{y}^s,t^s)$ and heading directions $\hat{h}_C^\star(t)$ of C, starting from $\mathbf{y}^s$, leading to $\mathbf{y}^f$ is first computed by solving

(3)–(8). Assuming that the size and orientation of the pattern do not change with time, it is then possible to predict the desired trajectories of each vehicle, using $\mathbf{X}^\star_C(t;\mathbf{y}^s,t^s)$ and $\hat{h}^\star_C(t)$. However, these trajectories may be infeasible, in part because of disparities among the flows encountered by the vehicles and by the center of mass (Lermusiaux et al., 2015).

Hence, $\hat{h}^\star_C(t)$ is only used as a first-guess for the heading directions of each vehicle. Starting from the current time $t \geq t^s$, the position of each vehicle at the next time-step is estimated by numerically integrating (1), with $F_P(t) = F$ and $\hat{h}(t) = \hat{h}^\star_C(t)$ (predictor step). The discrepancy between this predicted position and the desired position is used to correct the heading of each vehicle at time t (corrector step). (1) is integrated again using this updated heading direction to obtain the positions of the vehicles at the next time-step. This process is repeated until C reaches $\mathbf{y}^f$, thereby generating the complete trajectories of all vehicles. Finer algorithmic details may be found in Lolla (2012).

As for our reachability-based methodology (Section 4), the uncoupled nature of the computation of trajectories of C from that of individual vehicles allows for the trajectory of C to be optimized for several criteria (time-optimality, uncertainty minimization, etc.), independently of the maintenance of geometric patterns. However, the above method is only local: if the flow-fields experienced by vehicles in the formation are very different (e.g. when the pattern size is large compared to the scales of ocean currents), then, the desired pattern may not be maintained. This problem can persist even if other corrector schemes are employed (instead of first-order scheme discussed here). Moreover, in some cases, the vehicle trajectories may diverge so much from that of C that C may not be representative of the group any more.

References

Adalsteinsson, D., Sethian, J.A., 1995. A fast level set method for propagating interfaces. J. Comput. Phys. 118 (2), 269–277.

Adalsteinsson, D., Sethian, J.A., 1999. The fast construction of extension velocities in level set methods. J. Comput. Phys. 148 (1), 2–22.

Agarwal, A., Lermusiaux, P.F.J., 2011. Statistical field estimation for complex coastal regions and archipelagos. Ocean Model. 40 (2), 164–189.

Arkin, R.C., Balch, T., 1998. Cooperative multiagent robotic systems. In: Kortenkamp, D., Bonasso, R.P., Murphy, R. (Eds.), Artificial Intelligence and Mobile Robots. MIT Press, Cambridge, MA, USA, pp. 277–296.

Bahr, A., Leonard, J.J., Fallon, M.F., 2009. Cooperative localization for autonomous underwater vehicles. Int. J. Robot. Res. 28 (6), 714–728.

Bellingham, J.G., Rajan, K., 2007. Robotics in remote and hostile environments. Science 318 (5853), 1098–1102.

Bendjilali, K., Belkhouche, F., Belkhouche, B., 2009. Robot formation modelling and control based on the relative kinematics equations. Int. J. Robot. Automat. 24 (1), 79–85.

Beşiktepe, Ş.T., Lermusiaux, P.F.J., Robinson, A.R., 2003. Coupled physical and biogeochemical data-driven simulations of Massachusetts Bay in late summer: real-time and postcruise data assimilation. J. Mar. Syst. 40–41, 171–212.

Bleck, R., 2002. An oceanic general circulation model framed in hybrid isopycnic-cartesian coordinates. Ocean Model. 4 (1), 55–88.

Brown-Dymkoski, E., Kasimov, N., Vasilyev, O.V., 2014. A characteristic based volume penalization method for general evolution problems applied to compressible viscous flows. J. Comput. Phys. 262, 344–357.

Chaimowicz, L., Michael, N., Kumar, V., 2005. Controlling swarms of robots using interpolated implicit functions. In: 2005 IEEE International Conference on Robotics and Automation (ICRA), pp. 2487–2492.

Cherdron, W., Durst, F., Whitelaw, J.H., 1978. Asymmetric flows and instabilities in symmetric ducts with sudden expansions. J. Fluid Mech. 84 (1), 13–31.

Choi, H.L., How, J.P., 2010. Continuous trajectory planning of mobile sensors for informative forecasting. Automatica 46 (8), 1266–1275.

Colin, M.E.G.D., Duda, T.F., te Raa, L.A., van Zon, T., Haley Jr., P.J., Lermusiaux, P.F.J., Leslie, W.G., Mirabito, C., Lam, F.P.A., Newhall, A.E., Lin, Y.T., Lynch, J.F., 2013. Time-evolving acoustic propagation modeling in a complex ocean environment. In: OCEANS—Bergen, 2013 MTS/IEEE, pp. 1–9.

Consolini, L., Morbidi, F., Prattichizzo, D., Tosques, M., 2007. A geometric characterization of leader-follower formation control. In: 2007 IEEE International Conference on Robotics and Automation, pp. 2397–2402.

Cossarini, G., Lermusiaux, P.F.J., Solidoro, C., 2009. The lagoon of venice ecosystem: seasonal dynamics and environmental guidance with uncertainty analyses and error subspace data assimilation. J. Geophys. Res. 114, C0626.

Crandall, M.G., Lions, P.L., 1983. Viscosity solutions of hamilton-jacobi equations. Trans. Am. Math. Soc. 277, 1–43.

Curtin, T.B., Bellingham, J.G., 2009. Progress toward autonomous ocean sampling networks. Deep Sea Res. Part II: Top. Stud. Oceanogr. 56 (3), 62–67.

Curtin, T.B., Bellingham, J.G., Catipovic, J., Webb, D., 1993. Autonomous oceanographic sampling networks. Oceanography 6 (3), 86–94.

Cushman-Roisin, B., Beckers, J., 2010. Introduction to Geophysical Fluid Dynamics. Physical and Numerical aspects. Academic Press.

Derenick, J.C., Spletzer, J.R., 2007. Convex optimization strategies for coordinating large-scale robot formations. IEEE Trans. Robot. 23 (6), 1252–1259.

Desai, J.P., 2002. A graph theoretic approach for modeling mobile robot team formations. J. Robot. Syst. 19 (11), 511–525.

Dijkstra, H., Katsman, C., 1997. Temporal variability of the wind-driven quasi-geostrophic double gyre ocean circulation: basic bifurcation diagrams. Geophys. Astrophys. Fluid Dyn. 85, 195–232.

Dimarogonas, D.V., Tsiotras, P., Kyriakopoulos, K.J., 2009. Leader–follower cooperative attitude control of multiple rigid bodies. Syst. Control Lett. 58 (6), 429–435.

Durst, F., Melling, A., Whitelaw, J.H., 1974. Low Reynolds number flow over a plane symmetric sudden expansion. J. Fluid Mech. 64, 111–128.

Egbert, G.D., Erofeeva, S.Y., 2002. Efficient inverse modeling of barotropic ocean tides. J. Atmos. Oceanic Technol. 19 (2), 183–204.

Esin, Y.H., Unel, M., Yildiz, M., 2008. Formation control of multiple robots using parametric and implicit representations. In: Proceedings of the 4th international conference on Intelligent Computing: Advanced Intelligent Computing Theories and Applications—With Aspects of Artificial Intelligence. Springer-Verlag, Berlin, Heidelberg, pp. 558–565.

Fearn, R.M., Mullin, T., Cliffe, K.A., 1990. Nonlinear flow phenomena in a symmetric sudden expansion. J. Fluid Mech. 211, 595–608.

Fierro, R., Song, P., Das, A., Kumar, V., 2002. Cooperative control of robot formations. In: Cooperative Control and Optimization. In: Applied Optimization, 66. Springer, US, pp. 73–93.

Fiorelli, E., Leonard, N.E., Bhatta, P., Paley, D.A., Bachmayer, R., Fratantoni, D.M., 2004. Multi-AUV control and adaptive sampling in Monterey Bay. IEEE J. Oceanic Eng. 34, 935–948.

Gangopadhyay, A., Lermusiaux, P.F.J., Rosenfeld, L., Robinson, A.R., Calado, L., Kim, H.S., Leslie, W.G., Haley Jr., P.J., 2011. The California Current System: A multiscale overview and the development of a feature-oriented regional modeling system (FORMS). Dyn. Atmos. Oceans 52 (1–2), 131–169. (Special issue of Dynamics of Atmospheres and Oceans in honor of Prof. A.R. Robinson)

Gawarkiewicz, G., Jan, S., Lermusiaux, P.F.J., McClean, J.L., Centurioni, L., Taylor, K., Cornuelle, B., Duda, T.F., Wang, J., Yang, Y.J., Sanford, T., Lien, R.-C., Lee, C., Lee, M.-A., Leslie, W., Haley Jr., P.J., Niiler, P.P., Gopalakrishnan, G., Velez-Belchi, P., Lee, D.-K., Kim, Y.Y., 2011. Circulation and intrusions northeast of Taiwan: chasing and predicting uncertainty in the cold dome. Oceanography 24 (4), 110–121. http://dx.doi.org/10.5670/oceanog.2011.99.

Gordon, A.L., Sprintall, J., Ffield, A., 2011. Regional oceanography of the Philippine Archipelago. Oceanography 24 (1), 15–27.

Gordon, A.L., Villanoy, C.L., 2011, 24. Oceanography. Special issue on the Philippine Straits Dynamics Experiment. The Oceanography Society.

Hagen, P., Midtgaard, O., Hasvold, O., 2007. Making AUVs truly autonomous. In: OCEANS 2007, pp. 1–4.

Haley Jr., P.J., Agarwal, A., Lermusiaux, P.F.J., 2015. Optimizing velocities and transports for complex coastal regions and archipelagos. Ocean Model 89, 1–28. doi:10.1016/j.ocemod.2015.02.005.

Haley Jr., P.J., Lermusiaux, P.F.J., 2010. Multiscale two-way embedding schemes for free-surface primitive equations in the multidisciplinary simulation, estimation and assimilation system. Ocean Dyn. 60 (6), 1497–1537.

Haley Jr., P.J., Lermusiaux, P.F.J., Robinson, A.R., Leslie, W.G., Logoutov, O., Cossarini, G., Liang, X.S., Moreno, P., Ramp, S.R., Doyle, J.D., Bellingham, J., Chavez, F., Johnston, S., 2009. Forecasting and reanalysis in the Monterey Bay/California current region for the autonomous ocean sampling network-II experiment. Deep Sea Res. II 56 (3–5), 127–148.

Hodur, R.M., 1997. The naval research laboratory's coupled ocean/atmosphere mesoscale prediction system (coamps). Mon. Weather Rev. 125 (7), 1414–1430.

Høydalsvik, F., Mauritzen, C., Orvik, K., LaCasce, J., Lee, C., Gobat, J., 2013. Transport estimates of the western branch of the Norwegian Atlantic Current from glider surveys. Deep Sea Res. Part I: Oceanogr. Res. Pap. 79 (0), 86–95.

Hurlburt, H.E., Metzger, E.J., Sprintall, J., Riedlinger, S.N., Arnone, R.A., Shinoda, T., Xu, X., 2011. Circulation in the Philippine Archipelago simulated by 1/12° and 1/25° global HYCOM and EAS NCOM. Oceanography 24 (1), 28–47.

Jouvencel, B., Parodi, O., Xiang, X., 2010. Coordinated formation control of multiple autonomous underwater vehicles for pipeline inspection. Int. J. Adv. Robot. Syst. 7 (1), 75–84.

Leben, R.R., Born, G.H., Engebreth, B.R., 2002. Operational altimeter data processing for mesoscale monitoring. Mar. Geodesy 25 (1–2), 3–18.

Leonard, N.E., Fiorelli, E., 2001. Virtual leaders, artificial potentials and coordinated control of groups. In: Proceedings of the 40th IEEE Conference on Decision and Control, 2001, 3, pp. 2968–2973.

Leonard, N.E., Paley, D., Lekien, F., Sepulchre, R., Fratantoni, D., Davis, R., 2007. Collective motion, sensor networks, and ocean sampling. Proc. IEEE 95, 48–74. (special issue on the emerging technology of networked control systems).

Leonard, N.E., Paley, D.A., Davis, R.E., Fratantoni, D.M., Lekien, F., Zhang, F., 2010. Coordinated control of an underwater glider fleet in an adaptive ocean sampling field experiment in Monterey Bay. J. Field Robot. 27 (6), 718–740.

Lermusiaux, P.F.J., 1997. Error subspace data assimilation methods for ocean field estimation: theory, validation and applications. Harvard University (Ph.D. thesis).

Lermusiaux, P.F.J., 2007. Adaptive modeling, adaptive data assimilation and adaptive sampling. Phys. D: Nonlin. Phenom. 230, 172–196.

Lermusiaux, P.F.J., Chiu, C.-S., Gawarkiewicz, G.G., Abbot, P., Robinson, A.R., Miller, R.N., Jr., P.J.H., Leslie, W.G., Majumdar, S.J., Pang, A., Lekien, F., 2006. Quantifying uncertainties in ocean predictions. Oceanography 19 (1), 90–103.

Lermusiaux, P.F.J., Haley Jr., P.J., Leslie, W.G., Agarwal, A., Logutov, O., Burton, L.J., 2011. Multiscale physical and biological dynamics in the philippines archipelago: predictions and processes. Oceanography 24 (1), 70–89.

Lermusiaux, P.F.J., Haley Jr., P.J., Yilmaz, N.K., 2007. Environmental prediction, path planning and adaptive sampling: sensing and modeling for efficient ocean monitoring, management and pollution control. Sea Technol. 48 (9), 35–38.

Lermusiaux, P.F.J., Lolla, T., Haley Jr., P.J., Yigit, K., Ueckermann, M.P., Sondergaard, T., Leslie, W.G., 2015. Science of autonomy: time-optimal path planning and adaptive sampling for swarms of ocean vehicles. In: Curtin, T. (Ed.). Handbook of Ocean Engineering: Autonomous Ocean Vehicles, Subsystems and Control. Springer. (Chapter 11), in press.

Leslie, W.G., Robinson, A.R., Haley Jr., P., Logoutov, O., Moreno, P., Lermusiaux, P.F.J., Coehlo, E., 2008. Verification and training of real-time forecasting of multi-scale ocean dynamics for maritime rapid environmental assessment. J. Mar. Syst. 69 (1–2), 3–16.

Liu, S., Sun, D., Zhu, C., 2011. Coordinated motion planning for multiple mobile robots along designed paths with formation requirement. IEEE/ASME Trans. Mechatron. 16 (6), 1021–1031.

Logoutov, O.G., Lermusiaux, P.F.J., 2008. Inverse barotropic tidal estimation for regional ocean applications. Ocean Model. 25 (12), 17–34.

Lolla, T., 2012. Path planning in time dependent flows using level set methods. Department of Mechanical Engineering, Massachusetts Institute of Technology (Master's thesis).

Lolla, T., Haley Jr., P.J., Lermusiaux, P.F.J., 2014a. Time-optimal path planning in dynamic flows using level set equations: realistic applications. Ocean Dyn. 64 (10), 1399–1417.

Lolla, T., Lermusiaux, P.F.J., Ueckermann, M.P., Haley Jr., P.J., 2014b. Time-optimal path planning in dynamic flows using level set equations: theory and schemes. Ocean Dyn. 64 (10), 1373–1397.

Lolla, T., Ueckermann, M.P., Yigit, K., Haley Jr., P.J., Lermusiaux, P.F.J., 2012. Path planning in time dependent flow fields using level set methods. In: Proceedings of IEEE International Conference on Robotics and Automation, pp. 166–173.

Mallory, K., Hsieh, M.A., Forgoston, E., Schwartz, I.B., 2013. Distributed allocation of mobile sensing swarms in gyre flows. Nonlin. Process. Geophys. 20 (5), 657–668.

Michini, M., Hsieh, M., Forgoston, E., Schwartz, I., 2014. Robotic tracking of coherent structures in flows. IEEE Trans. Robot. 30 (3), 593–603.

Mittal, R., Iaccarino, G., 2005. Immersed boundary methods. Annu. Rev. Fluid Mech. 37, 239–261.

MSEAS Group, 2010. Multidisciplinary simulation, estimation, and assimilation systems manual. MSEAS Report. MIT.Cambridge, MA, USA. http://mseas.mit.edu/, http://mseas.mit.edu/codes.

Olfati-Saber, R., Murray, R., 2002. Graph rigidity and distributed formation stabilization of multi-vehicle systems. In: Proceedings of the 41st IEEE Conference on Decision and Control, 2002, 3, pp. 2965–2971. doi:10.1109/CDC.2002.1184307.

Onken, R., Álvarez, A., Fernández, V., Vizoso, G., Basterretxea, G., Tintoré, J., Haley Jr., P.J., Nacini, E., 2008. A forecast experiment in the Balearic sea. J. Mar. Syst. 71 (1–2), 79–98.

Osher, S., Fedkiw, R., 2003. Level Set Methods and Dynamic Implicit Surfaces. Springer Verlag.

Paley, D.A., Zhang, F., Leonard, N.E., 2008. Cooperative control for ocean sampling: the glider coordinated control system. IEEE Trans. Control Syst. Technol. 16 (4), 735–744.

Pimenta, L., Pereira, G., Michael, N., Mesquita, R., Bosque, M., Chaimowicz, L., Kumar, V., 2013. Swarm coordination based on smoothed particle hydrodynamics technique. IEEE Trans. Robot. 29 (2), 383–399.

Qu, T., Lukas, R., 2003. The bifurcation of the north equatorial current in the pacific. J. Phys. Oceanogr. 33 (1), 5–18.

Ramp, S., Lermusiaux, P.F.J., Shulman, I., Chao, Y., Wolf, R.E., Bahr, F.L., 2011. Oceanographic and atmospheric conditions on the continental shelf north of the Monterey Bay during August 2006. Dyn. Atmos. Oceans 52 (1–2), 192–223.

Ramp, S.R., Davis, R.E., Leonard, N.E., Shulman, I., Chao, Y., Robinson, A.R., Marsden, J., Lermusiaux, P.F.J., Fratantoni, D.M., Paduan, J.D., Chavez, F.P., Bahr, F.L., Liang, S., Leslie, W., Li, Z., 2009. Preparing to predict: The second autonomous ocean sampling network experiment in the Monterey Bay. Deep Sea Res. Part II: Top. Stud. Oceanogr. 56 (35), 68–86.({AOSN} II: The Science and Technology of an Autonomous Ocean Sampling Network)

Reed, B., Hover, F., 2014. Oceanographic pursuit: networked control of multiple vehicles tracking dynamic ocean features. Methods Oceanogr. 10, 21–43. (Special Issue: Autonomous Marine Vehicles

Reed, B.L., Hover, F.S., 2013. Tracking ocean fronts with multiple vehicles and mixed communication losses. In: 2013 IEEE/RSJ International Conference on Intelligent Robots and Systems (IROS), pp. 3374–3381.

Reif, J.H., Wang, H., 1999. Social potential fields: A distributed behavioral control for autonomous robots. Robot. Autonom. Syst. 27, 171–194.

Ren, W., Beard, R.W., Beard, A.W., 2003. Decentralized scheme for spacecraft formation flying via the virtual structure approach. AIAA J. Guid., Control, Dyn. 27, 73–82.

Ren, W., Sorensen, N., 2008. Distributed coordination architecture for multi-robot formation control. Robot. Autonom. Syst. 56 (4), 324–333.

Roth, B., 1981. Rigid and flexible frameworks. Am. Math. Mon. 88 (1), 6–21.

Rudnick, D.L., Davis, R.E., Eriksen, C.C., Fratantoni, D.M., Perry, M.J., 2004. Underwater gliders for ocean research. Mar. Technol. Soc. J. 38 (2), 73–84.

Sabattini, L., Secchi, C., Fantuzzi, C., 2011. Arbitrarily shaped formations of mobile robots: artificial potential fields and coordinate transformation. Auton. Robots 30 (4), 385–397.

Schmidt, H., Bellingham, J., Johnson, M., Herold, D., Farmer, D., Pawlowicz, R., 1996. Real-time frontal mapping with AUVs in a coastal environment. In: MTS/IEEE Conference Proceedings on Prospects for the 21st Century (OCEANS'96), 3, pp. 1094–1098.

Schofield, O., Glenn, S., Orcutt, J., Arrott, M., Meisinger, M., Gangopadhyay, A., Brown, W., Signell, R., Moline, M., Chao, Y., Chien, S., Thompson, D., Balasuriya, A., Lermusiaux, P., Oliver, M., 2010. Automated sensor network to advance ocean science. Eos, Trans. Am. Geophys. Union 91 (39), 345–346.

Sethian, J.A., 1999. Level Set Methods and Fast Marching Methods: Evolving Interfaces in Computational Geometry, Fluid Mechanics, Computer Vision, and Materials Science. Cambridge University Press: Cambridge, U.K..

Shimone, T., Kurabayashi, D., Okita, K., Funato, T., 2008. Implementation of formation transition system using synchronization in a mobile robot group. In: Laugier, C., Siegwart, R. (Eds.), Field and Service Robotics. In: Springer Tracts in Advanced Robotics, 42. Springer, Berlin/Heidelberg, pp. 423–432.

Simmonet, E., Dijkstra, H., Ghil, M., 2009. Bifurcation analysis of ocean, atmosphere, and climate models. Computational Methods for the Atmosphere and the Oceans. Handbook of Numerical Analysis, XIV, pp. 187–229.

Sisto, M., Gu, D., 2006. A fuzzy leader-follower approach to formation control of multiple mobile robots. In: 2006 IEEE/RSJ International Conference on Intelligent Robots and Systems, pp. 2515–2520.

Smith, R.N., Schwager, M., Smith, S.L., Jones, B.H., Rus, D., Sukhatme, G.S., 2011. Persistent ocean monitoring with underwater gliders: adapting sampling resolution. J. Field Robot. 28 (5), 714–741.

Subramani, D.N., Lolla, T., Haley Jr., P.J., Lermusiaux, P.F.J., 2015. A stochastic optimization method for energy-based path planning. In: Ravela, S., Sandu, A. (Eds.), In: Dyamic Data-driven Environmental Systems Science Conference. In: Lecture Notes in Computer Science. Springer International Publishing. in press.

Švestka, P., Overmars, M.H., 1998. Coordinated path planning for multiple robots. Robot. Autonom. Syst. 23 (3), 125–152.

Swaminathan, K., Minai, A.A., 2005. Stigmergic Optimization. Spring-Verlag.

Ueckermann, M.P., Lermusiaux, P.F.J., 2011. 2.29 Finite Volume MATLAB framework documentation. Technical Report. MSEAS Group, Massachusetts Institute of Technology, Cambridge, MA USA.

Ueckermann, M.P., Lermusiaux, P.F.J., Sapsis, T.P., 2013. Numerical schemes for dynamically orthogonal equations of stochastic fluid and ocean flows. J. Comput. Phys. 233, 272–294.

Van Leer, B., 1977. Towards the ultimate conservative difference scheme. IV. A new approach to numerical convection. J. Comput. Phys. 23 (3), 276–299.

Wagner, G., Choset, H., 2011. M*: A complete multirobot path planning algorithm with performance bounds. In: 2011 IEEE/RSJ International Conference on Intelligent Robots and Systems (IROS), pp. 3260–3267. doi:10.1109/IROS.2011.6095022.

Wang, D., Lermusiaux, P.F.J., Haley Jr., P.J., Eickstedt, D., Leslie, W.G., Schmidt, H., 2009. Acoustically focused adaptive sampling and on-board routing for marine rapid environmental assessment. J. Mar. Syst. 78, S393–S407.

Xu, J., Lermusiaux, P.F.J., Haley, P.J., Leslie, W.G., Logoutov, O.G., 2008. Spatial and temporal variations in acoustic propagation during the PLUSNet07 exercise in Dabob Bay. Proceedings of Meetings on Acoustics (POMA), 155th Meeting Acoustical Society of America 4, 070001.

Yang, H., Zhang, F., 2010. Geometric formation control for autonomous underwater vehicles. In: Proceedings of 2010 International Conference on Robotics and Automation, pp. 4288–4293. Anchorage, AL.

Yigit, K., 2011. Path planning methods for autonomous underwater vehicles. Department of Mechanical Engineering, Massachusetts Institute of Technology Master's thesis.

Yuh, J., 2000. Design and control of autonomous underwater robots: a survey. Autonom. Robots 8 (1), 7–24.

Zhang, F., Fratantoni, D.M., Paley, D., Lund, J., Leonard, N.E., 2007. Control of coordinated patterns for ocean sampling. Int. J. Control 80 (7), 1186–1199.

Zhang, F., Leonard, N.E., 2007. Coordinated patterns of unit speed particles on a closed curve. Syst. Control Lett. 56 (6), 397–407.